

A Catalog of Molecular Clumps and Cores with Infall Signatures

Shuling Yu^{1,2}, Zhibo Jiang^{1,2,3}, Yang Yang^{1,2}, Zhiwei Chen¹ and Haoran Feng^{1,2}

¹ Purple Mountain Observatory, Chinese Academy of Sciences, Nanjing, Jiangsu 210023, People's Republic of China; zbjiang@pmo.ac.cn

² University of Science and Technology of China, Chinese Academy of Sciences, Hefei, Anhui 230026, People's Republic of China

³ China Three Gorges University, Yichang, Hubei 443002, People's Republic of China

Received 20xx month day; accepted 20xx month day

Abstract The research of infall motion is a common means to study molecular cloud dynamics and the early process of star formation. Many works had been done in-depth research on infall. We searched the literature related to infall study of molecular cloud since 1994, summarized the infall sources identified by the authors. A total of 456 infall sources are catalogued. We classify them into high-mass and low-mass sources, in which the high-mass sources are divided into three evolutionary stages: prestellar, protostellar and HII region. We divide the sources into clumps and cores according to their sizes. The H₂ column density values range from 1.21×10^{21} to $9.75 \times 10^{24} \text{ cm}^{-2}$, with a median value of $4.17 \times 10^{22} \text{ cm}^{-2}$. The H₂ column densities of high-mass and low-mass sources are significantly separated. The median value of infall velocity for high-mass clumps is 1.12 km s^{-1} , and the infall velocities of low-mass cores are virtually all less than 0.5 km s^{-1} . There is no obvious difference between different stages of evolution. The mass infall rates of low-mass cores are between 10^{-7} and $10^{-4} M_{\odot} \text{yr}^{-1}$, and those of high-mass clumps are between 10^{-4} and $10^{-1} M_{\odot} \text{yr}^{-1}$ with only one exception. We do not find that the mass infall rates vary with evolutionary stages.

Key words: stars: formation — ISM: kinematics and dynamics — ISM: molecules — radio lines: ISM

1 INTRODUCTION

Infall motion is the initial stage of star formation. Although stars with different masses may have different formation mechanisms (e.g., Cesaroni et al. 2007; Zinnecker & Yorke 2007; Beltrán & de Wit 2016; Klassen et al. 2016), they all start from the collapse and infall of molecular cloud cores. Low-mass stars are believed to formed through inside-out gravitational collapse of dense molecular cores (Shu 1987), in which gravity overcomes thermal and nonthermal (mainly magnetic and turbulent) pressure (Zhou et al. 1993; Zhou et al. 1994). For high-mass stars ($\geq 8 M_{\odot}$), the formation mechanism is still controversial because of the poverty of samples and the difficulty of observation due to the larger distance of star-forming region, stronger interaction with surrounding molecular clouds, and shorter star-forming timescale. There are two dominant models, one is core accretion (Yorke & Sonnhalter 2002; McKee & Tan 2002, 2003), which assumes that massive stars form as their population of low-mass stars in

isolation, but that the accretion rate is a few orders of magnitude higher than low-mass stars. Another model is called competitive accretion (Bonnell & Bate 2002; Bonnell et al. 2004). This model claims that massive stars form in the dense part of molecular clumps (size $\leqslant 1$ pc and mass $\geqslant 200 M_{\odot}$, Beuther et al. 2005; Tan et al. 2014). They compete to accrete materials with other protostars, and the accretion continues until the accretion condition is not satisfied. Some recent observations (e.g., Liu et al. 2013; Peretto et al. 2013; Contreras et al. 2018) support this model. In any case, infall motion is the key to initiating the formation of massive stars and maintaining accretion flows to increase mass continually during subsequent phases of evolution in these two models.

The method of finding infall samples is to identify them through special line profile. One of the significant features of infall motion is called “the spectral line asymmetry” (e.g., Zhou 1992; Mardones et al. 1997; Lee et al. 1999; Evans 1999; Wu & Evans II 2003; Churchwell et al. 2010), i.e. it shows double peaks profile where the blue peak is stronger than the red one on an optically thick line, while the optically thin line has only a single peak between the double peaks of the optically thick line. The commonly used optically thick lines are CO(1-0), HCO⁺(1-0), HCO⁺(4-3), HCN(1-0), CS(2-1), H₂CO(2-1), etc. Their isotopic molecular line, C¹⁸O(1-0), H¹³CO⁺(1-0), H¹³CO⁺(4-3), H¹³CO⁺(3-2), H¹³CN(1-0), are generally used as optically thin line to trace the system velocity. In addition, N₂H⁺(1-0) is generally optically thin, and can characterize the dense inner region of a core and well estimate the system velocity (Mardones et al. 1997; Lee et al. 1999), so it is particularly suitable for studying the structure and kinematics of star-forming cores and has been used to detect infall in IRDCs (infrared dark clouds), starless cores and protostar cores (e.g., Lee et al. 2001; Fuller et al. 2005; Keto et al. 2015; Keown et al. 2016; Storm et al. 2016; Kim et al. 2021).

At present, there are good constraints on the formation of low-mass stars, and the corresponding evidence of infall motion has been found in the early stage until class I phase (e.g., Mardones et al. 1997; Gregersen 2000; Lee et al. 2001; Lee & Myers 2011; Padoan et al. 2014; Keown et al. 2016; Kim et al. 2021). In contrast, due to the controversy on the formation mechanism, the infall observation and research of high-mass young stellar objects (YSOs) has become more popular in recent years (e.g., Sridharan et al. 2002; Fuller et al. 2005; Klaassen & Wilson 2008; Klaassen et al. 2012; Sun & Gao 2009; Reiter et al. 2011; Liu et al. 2011; Qiu et al. 2012; Liu et al. 2013; He et al. 2016; Qin et al. 2016; Cunningham et al. 2018; Saral et al. 2018; Tang et al. 2019; Liu et al. 2020; Yang et al. 2020b; Yue et al. 2021). Rygl et al. (2013) found that the formation are closely related to the “clump-to-cloud” column density ratio. They did not find YSOs in clumps with molecular hydrogen column density less than $4 \times 10^{22} \text{ cm}^{-2}$; this ratio greater than 2 is the first sign of the beginning of star formation, and infall signature can be widely observed at this time; when the ratio greater than 3, the infall motions stop in most clumps. He et al. (2015, 2016) analysed 732 high-mass clumps, and concluded that the detection rate of infall sources decreases gradually from prestellar to protostar and then to HII region phase; the mass of the clumps increase with these evolutionary stages whether the infall is detected or not. However, Klaassen et al. (2012) came to an abnormal situation that the detection rate of infall candidates increased significantly from protostar to hypercompact HII region phase. He thought this may be related to the beam dilution caused by smaller infall area of younger sources. Yue et al. (2021) observed 30 high-mass clumps associated with bright infrared sources, and found that the clumps with higher mass and luminosity tend to have larger mass infall rates. Large sample survey and high resolution observation of interferometric array have become the future trend of infall study.

On the basis of observation and theoretical study, the process of massive star formation is proposed by a number of researchers. Saral et al. (2018) used the classification method summarized by Motte et al. (2018): (1) starless core (Lee et al. 2001; Sohn et al. 2007; Lee & Myers 2011; Schnee et al. 2013), the gravitationally bound prestellar core or IRDC (Contreras et al. 2018); (2) hot molecular core (HMC) or

protostellar (Mardones et al. 1997; Wu et al. 2005; Fuller et al. 2005; Keown et al. 2016); (3) HII region (He et al. 2016). An additional stage is defined by Guzmán et al. (2015). At this stage, the expansion of the ionized gas finally destroys the molecular envelope, forming the characteristic of an extended classical H II region and a photodissociation region (PDR). Because HII still exists in this stage, but it is merely more extended, so we incorporate this stage into the stage 3. Therefore, this paper adopts the classification by Motte et al. (2018), which is divided into three main stages: prestellar, protostellar, HII region.

For simplicity, we define the infall source as source with infall signature in this paper. There is no complete statistical work on infall sources before. Therefore we make a comprehensive search of infall study in the literature, aggregate the infall sources into a catalog, and make some statistical analysis on the physical properties.

2 THE DATA

2.1 Tracers

Table 1 lists the optically thick and thin lines used to identify the infall signatures collected in this paper. The frequencies and upper level of energies (E_u) in the catalogue are obtained from the Splatatalogue Database¹. The critical density (n_{crit}) of each molecular transition is calculated by $n_{\text{crit}} = A_{ul}/\gamma_{ul}$, where A_{ul} is the Einstein A-coefficient and γ_{ul} is the collision rate coefficient for collisions with H₂ at a certain temperature. The Leiden Atomic and Molecular Database² (LAMDA, Schöier et al. 2005) provide A_{ul} and γ_{ul} at different temperatures. We adopt those which are nearest E_u .

Different spectral lines can trace different properties. HCO⁺ is an abundant molecule, with particularly enhanced abundances around higher fractional ionized regions (Vasyunina et al. 2011). HCN is a good tracer of infall motion in the low-mass star-forming region. However, it may become unreliable because of a higher level of turbulence (Redman et al. 2008) and outflow signatures (Zhang et al. 2007) for the high-mass cores (Vasyunina et al. 2011). HNC is also a commonly used infall tracer. The abundance ratio HCN/HNC strongly depends on the temperature, it decreases from decades near the warm core to ~ 1 on the colder edges (Sarrasin et al. 2010).

Table 2 lists the number of sources observed by each spectral line. The upper part is the optically thick line. About 77% of the infall sources are identified with HCO⁺ (1-0), HNC (1-0) is the second most (28%). This may be because HCO⁺ (1-0) and HNC (1-0) have moderate critical density, which are high enough to trace the dense part closer to the core, and are not as high as CS (2-1), which makes it difficult to achieve such environmental conditions. In addition, the frequency of HCO⁺ (1-0) and HNC (1-0) fall in one of the best windows of atmospheric transparency, allowing them to be easily observed. Smith et al. (2013) modelled the emission produced by the hydrodynamic simulation of collapsing clouds in massive star-forming regions without outflows, and concluded that HCO⁺ (1-0) is better performed to trace collapse than HCO⁺ (4-3). Some infall studies (e.g., Fuller et al. 2005; Vasyunina et al. 2011; Rygl et al. 2013; Cunningham et al. 2018; Yuan et al. 2018; Zhang et al. 2018) that simultaneously observe multiple optically thick lines seem to support HCO⁺ (1-0) as a more effective tracer. But note that this may not be always true, for example, Tsamis et al. (2008) shows that HCO⁺ (4-3) may be a better tracer to detect the asymmetry than HCO⁺ (1-0) at earlier times.

The observation of optically thin lines is also particularly crucial. Multiple velocity component, for example, the colliding fragments of two clouds, could produce the double-peaked blue profile, but they would also produce a double-peaked profile in the optically thin line (Evans 1999). In order to eliminate this situation, the optically thin line must have only a single peak between the two peaks of the optically

¹ <https://splatalogue.online>

² <https://home.strw.leidenuniv.nl/~moldata/>

thick line. The lower part of table 2 list the optically thin lines used in the articles. Different line widths of optically thin lines will affect the estimation of skewness parameters, see section 3.4.

Table 1: Tracers Used in the Literature

Serial Number	Spectral line	Transition	Rest Frequency ^a (GHz)	E_u ^a (K)	n_{crit} ^b (cm ⁻³)
optically thick lines					
1	HCO ⁺	J = 1-0	89.188526	4.28	1.6×10^5
2	HCO ⁺	J = 3-2	267.557633	25.68	3.7×10^6
3	HCO ⁺	J = 4-3	356.734242	42.80	9.3×10^6
4	CO	J = 2-1	230.538000	16.60	1.1×10^4
5	CO	J = 3-2	345.795990	33.19	3.7×10^4
6	CO	J = 4-3	461.040768	55.32	9.1×10^4
7	HNC	J = 1-0	90.663564	4.35	2.8×10^5
8	HNC	J = 4-3	362.630304	43.51	2.0×10^7
9	HCN	J = 1-0	88.631602	4.25	1.0×10^6
10	HCN	J = 3-2	265.886434	25.52	6.8×10^7
11	CS	J = 2-1	97.980953	7.05	3.3×10^7
12	H ₂ CO	$J_{kk'} = 2_{12}-1_{11}$	140.839518	21.9	7.7×10^5
13	CN	N = 2-1,J=3/2-1/2,F=5/2-3/2	226.659558	16.31	1.3×10^7
14	C ¹⁸ O	J = 2-1	219.560358	15.81	9.3×10^3
15	¹³ CO	J = 3-2	330.587965	31.73	3.3×10^4
16	CH ₃ CN	J=19-18 K=3	349.393297	232.0	1.6×10^7
optically thin lines					
1	N ₂ H ⁺	J = 1-0	93.173404	4.47	1.4×10^5
2	H ¹³ CO ⁺	J = 1-0	86.754288	4.16	1.5×10^5
3	H ¹³ CO ⁺	J = 3-2	260.255339	24.98	3.2×10^6
4	C ¹⁸ O	J = 1-0	109.782176	5.27	1.9×10^3
5	C ¹⁸ O	J = 2-1	219.560358	15.81	9.3×10^3
6	C ¹⁷ O	J = 3-2	337.061130	32.35	3.5×10^4

Notes: *a*: The rest frequency of the line and upper level of energy values are obtained from the splatalogue database. *b*: the critical density are derived from the formula $n_{\text{crit}} = A_{ul}/\gamma_{ul}$.

2.2 The Catalog

Up to May 2021, a total of 456 infall candidates have been identified, including 352 (77%) sources being associated with high-mass star-forming regions, and 55 (12%) with low mass, the remaining 49 (11%) being uncertain. The low-mass sources are fewer, probably due to the more attention has been paid to high-mass sources in recent years, meanwhile the weakness of infall characteristics of low-mass sources. Of these sources, eight are observed by interferometric array, accounting for a small proportion and will not be discussed separately, the others are observed by single-dish telescope.

We divide the sources into clumps and cores as their properties may be different in infall motion. He et al. (2015) counted the sources and found that more than 96.6 per cent of clumps have masses higher than $100 M_{\odot}$. Saral et al. (2018) thought that the dense cores have sizes <0.1 pc and masses $<100 M_{\odot}$. This paper adopts such a grouping criterion: when the radius of a source lower than 0.1pc (main criteria) and mass lower than $100 M_{\odot}$, we believe this source is a core, otherwise, it is classified as a clump. For

Table 2: The Number of Sources Observed by Tracers

Serial Number	Spectral Line	Number of Sources	Reference
optically thick lines			
1	HCO ⁺ (1-0)	350	3,5,10,12,13,14,15,16,17,18,19,20,21,27,28
2	HCO ⁺ (3-2)	30	2,6,7,9,19,20,22,23,24, 25,27,30,31
3	HCO ⁺ (4-3)	18	13,22,23,27,30
4	CO(2-1)	24	13
5	CO(3-2)	8	13
6	CO(4-3)	18	1,29
7	HNC(1-0)	129	12,28
8	HNC(4-3)	1	22,23,30
9	HCN(1-0)	48	3,26,31
10	HCN(3-2)	8	5,9,11,14,15,19,20
11	CS(2-1)	24	6,19,20,21,22,23,24,30,31
12	H ₂ CO(2 ₁₂ -1 ₁₁)	26	22,23,27,30
13	CN(N = 2-1,J=3/2-1/2,F=5/2-3/2)	3	5,8,10,14,16,20
14	C ¹⁸ O(2-1)	1	7
15	¹³ CO(3-2)	1	10,14,16,20
16	CH ₃ CN(J=19-18,K=3)	1	4
optically thin lines			
1	N ₂ H ⁺ (1-0)	304	6,12,22,26,27,28
2	H ¹³ CO ⁺ (1-0)	56	13,14
3	H ¹³ CO ⁺ (3-2)	32	19,25,27
4	C ¹⁸ O(1-0)	77	3,6,20
5	C ¹⁸ O(2-1)	33	13
6	C ¹⁷ O(3-2)	18	1

Notes: references are: 1: [Yue et al. \(2021\)](#), 2: [Contreras et al. \(2018\)](#), 3: [Yang et al. \(2020a\)](#), 4: [Liu et al. \(2020\)](#), 5: [Liu et al. \(2013\)](#), 6: [Lee et al. \(2001\)](#), 7: [Tang et al. \(2019\)](#), 8: [Qiu et al. \(2012\)](#), 9: [Qin et al. \(2016\)](#), 10: [Wu et al. \(2009\)](#), 11: [Liu et al. \(2011\)](#), 12: [He et al. \(2015, 2016\)](#), 13: [Rygl et al. \(2013\)](#), 14: [Klaassen et al. \(2012\)](#), 15: [Klaassen & Wilson \(2007\)](#), 16: [Klaassen & Wilson \(2008\)](#), 17: [Sridharan et al. \(2002\)](#), 18: [Kurtz et al. \(1994\)](#), 19: [Reiter et al. \(2011\)](#), 20: [Sun & Gao \(2009\)](#), 21: [Shirley et al. \(2003\)](#), 22: [Mardones et al. \(1997\)](#), 23: [Su et al. \(2019\)](#), 24: [Lee & Myers \(2011\)](#), 25: [GregerSEN et al. \(1997\); GregerSEN \(2000\)](#), 26: [Kim et al. \(2021\)](#), 27: [Fuller et al. \(2005\)](#), 28: [Saral et al. \(2018\)](#), 29: [Faúndez et al. \(2004\)](#), 30: [Di Francesco et al. \(2001\)](#), 31: [Keown et al. \(2016\)](#).

those sources whose radius data are not given in the literature, we use the calculated distance and the spatial resolution of the telescope to estimate the radius. Of all the 456 sources, 396 (87%) are clumps and 60 (13%) are cores. For 352 high-mass sources, 343 (97%) are clumps, and for 54 low-mass sources, 46 (85%) are cores. That is, vast majority of the high-mass sources are clumps, and most of the low-mass sources are cores. Therefore, we ignore the influence of these few parts and only discuss the statistical properties of high-mass clumps and low-mass cores. The difference of statistical result is less than 5% when the samples are roughly divided into high-mass and low-mass sources compared with which are grouped into clumps and cores.

Table 3 lists the first ten sources of the infall catalog and their physical parameters. The complete catalog is in the appendix A.1. All the parameters are fetched from the literature, except the distance. The columns are as following:

- (1): internal serial number. Source that observed by interferometric array are signed with * in the upper right. The symbol † in the upper left indicates that the source is considered as a core, and the rest are clumps;
- (2)(3): the right ascension and declination (J2000);
- (4): the alias names of sources based on Galactic Coordinate;

- (5): the distance of each source, which are calculated by the parallax-based distance estimator³ (Reid et al. 2016, 2019). It used the Bayesian approach to assign sources to spiral arms based on their (l , b , v) coordinates with respect to arm signatures seen in CO and HI surveys. The estimator gives two most likely values of distance from the full distance probability density function, and use the parameter P to control the prior probability of obtaining a near/far distance. We also calculated the scale hight of each source by using the maximum likelihood distance. We found that for some sources, the scale hight will be much larger than that of molecular gas disk, that is, ~ 280 pc (Su et al. 2021). In such cases the near distance is adopted, although the probability of the far distance given by the estimator is greater;
- (6): the velocity corresponding to the peak position of the optically thin line. Some sources have been observed by more than one groups, they may give different parameters in such cases, we adopt the most recent one. This applies to columns 6 to 13, except column 10;
- (7)(8): the column density and number density (assumed to be spherical) of H₂;
- (9): mass;
- (10): optically thick lines that show blue asymmetry. The number is the same as that in table 1, and the bold font indicate the one being used to calculate δv ;
- (11): measure of asymmetry of the spectral profile. If multiple optically thick lines are used to identify infall motion, and multiple values are obtained accordingly, then we choose the one considered to be most effective in the paper, see section 3.4;
- (12): infall velocity;
- (13): mass infall rate;
- (14): the mass type of the source, *high* and *low* denote high-mass and low-mass, respectively;
- (15): evolutionary stage. The number 1, 2, 3 refer to stages of prestellar, protostellar and HII region for high-mass sources and 1, 2 for low-mass ones. Sources labelled as CHII (compact HII) or HCHII (hyper-compact HII) or UCHII (ultra-compact HII) in the literature are all merged into category 3 in this work;
- (16): The maser associated with these sources in the range of 1'. The number 1, 2, 3, 4 represent the maser of CH₃OH-I, CH₃OH-II, H₂O, OH, respectively;
- (17): The sources associated with outflow provided in some literature (Wu et al. 2004; Maud et al. 2015; Li et al. 2019; Zhang et al. 2020) within 2';
- (18): references. The number is the same as listed in table 2. The angular resolution and sensitivity of adopted observations are listed below according to the sequence of references. 1: 13'', 0.19 K at 0.27 km s⁻¹ for CO (4-3) and 0.14 K at 0.27 km s⁻¹ for C¹⁷O (3-2), 2: 1.2'', 0.14 K at 0.08 km s⁻¹, 3: 62'', 0.1 K at 0.2 km s⁻¹, 4: 0.14'', 5: 18.3'', 0.15 K for HCN (3-2), 6: 52'', 7: 3.74'' \times 3.04'' (-86°) for C¹⁸O (2-1), 0.86'' \times 0.86'' (85°) for HCO⁺(3-2), 8: 1.4'' \times 1.3'' (57°) for CN (N=2-1), 9: 2.3'' \times 2.1'' (-60°), 11: 1.63'' \times 1.28'' (-81.4°), 12: 19.2'', 13: 28'', 0.10 K at 0.08 km s⁻¹ for HCO⁺(1-0), and 11'', 1.3 K at 1.5 km s⁻¹ for CO (2-1), 14: 15'', 0.1 K at 0.42 km s⁻¹ (356 GHz) and 0.07 K at 0.82 km s⁻¹ (347 GHz), 15: 14'', 0.13 K at 0.53 km s⁻¹, 16: 14'', 0.13 K at 0.42 km s⁻¹, 19: 18'', 20: 55'', \sim 0.07 K, 21: 24.5'', 22: 28'', 23: 16.55'', 24: 52'', 25: 26'', 26: 32'', \sim 0.4 K at 0.11 km s⁻¹, 27: 29'' (IRAM), 14'' (JCMT), 0.08 K for HCO⁺(4-3) and 0.07 K for HCO⁺(1-0), 28: 38'', 29: 24'', 30: \sim 2'', 31: 9.4'', 0.02 K at 0.044 km s⁻¹.

Table 3: The Catalog of All Collected Infall Sources

No.	R.A. (J2000)	Dec. (J2000)	Alias	Dist. (kpc)	V_{LSR} (km s $^{-1}$)	$N(\text{H}_2)$ (cm $^{-2}$)	$n(\text{H}_2)$ (cm $^{-3}$)	Mass (M $_{\odot}$)	Lines	δv	V_{in} (km s $^{-1}$)	\dot{M}_{in} (M $_{\odot}$ yr $^{-1}$)	Type	Stage	Maser	Outflow	Ref
(1)	(2)	(3)	(4)	(5)	(6)	(7)	(8)	(9)	(10)	(11)	(12)	(13)	(14)	(15)	(16)	(17)	(18)
1	00:35:40.1	+66:14:23	G121.34+3.42	0.18	-5.3	9.8E+21			1,9	-0.47							3
2	00:36:47.5	+63:29:01	G121.30+0.66	0.9	-17.6				2	-0.54			high		123	Y	19
3	00:36:53.6	+63:28:03	G121.31+0.64	1.1	-17.3	1.7E+22			1,9	-0.63	0.29	1.6E-3		2			3
4	00:52:25.1	+56:33:54	G123.07-6.31	2.2	-30.4				1,2,10	-0.20			high	3	123	Y	19,20
5	02:19:51.8	+61:03:26	G133.42+0.00	0.9	-15.2	4.8E+21			9	-0.59				2			3
6	02:27:03.8	+61:52:25	W3(OH)	2.4	-48.0		6.0E+6		1,10	-0.23	0.06	3.0E-4	high	3	1234	Y	14,15,19,20
^{†7*}	02:27:04.7	+61:52:26	W3(H ₂ O)	2.0	-47.8	2.6E+24	1.0E+8	2.6E+1	2,10	-0.65	2.70	2.3E-3	high	2	1234	Y	9
^{†8}	02:53:12.2	+68:55:52	LDN 1355	0.3	-3.8	1.4E+21	9.1E+3		11	-0.42	0.12	8.4E-6	low	1			6,24
^{†9}	03:26:37.0	+30:15:26	IRAS03235+3004	0.35	4.9				2	-0.66			low	2	3		25
^{†10}	03:28:32.5	+31:11:05	J03283258+3111040	0.3	7.2				9	-0.45	0.17	6.5E-6	low	2			26

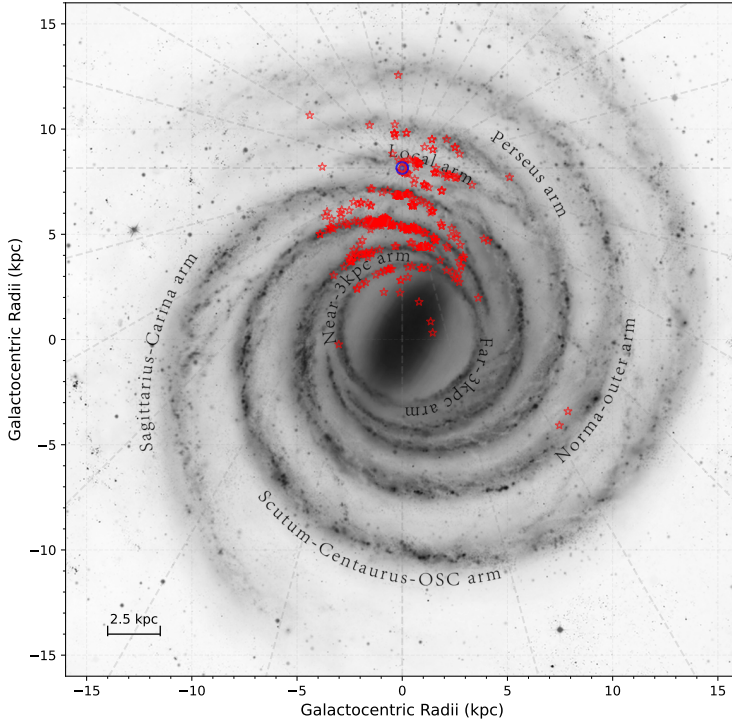


Fig. 1: Galactic distribution of the infall sources. The blue circle indicates the location of the Sun. The red pentagram represents the location of the infall sources. The background is the imaginary face-on image of the Milky Way (created: “Xing-Wu Zheng & Mark Reid BeSSeL/NJU/CFA”).

3 STATISTICS AND DISTRIBUTION

3.1 Spatial Distribution

Figure 1 shows the galactic distribution of all infall sources overlaid on the imaginary face-on image of the Milky Way, which is adopted from “Xing-Wu Zheng & Mark Reid BeSSeL/NJU/CFA⁴”, and which is believed to be currently the most scientifically accurate visualization of the Milky Way. The blue circle indicates the location of the Sun, with a distance 8.15 kpc to the Galactic center (Reid et al. 2019). The red pentagram represents the location of the infall sources. The scale of the image is indicated at lower left corner of the figure. We found that most of the sources (about 90%) are located within 5 kpc of the Sun. This may be caused by the observation effect. Moreover, The numbers of infall sources

³ <http://bessel.vlbi-astrometry.org/node/378>

⁴ <https://astronomy.nju.edu.cn/xtzl/EN/>

inside and outside the solar circle are 390 and 66, respectively. Although the observations to date are far from complete, the present evidence shows that the star formation activity inside the solar circle is more intense than the outside (Djordjevic et al. 2019), which needs further investigation in the future. Some infall sources are distributed on the spurs between the Local and Sagittarius arms (Xu et al. 2016) and between the Sagittarius and Scutum arms.

3.2 Excitation Temperature

The excitation temperature T_{ex} is usually estimated using the standard radiation transfer equation and assuming local thermodynamic equilibrium (LTE).

Of all the sources, there are 109 that have valid T_{ex} values, all of them are fetched from the literature. we don't differentiate these sources by high mass or low mass because of the relatively small number. The median and mean value of T_{ex} are 12.3 K and 13.4 K respectively. Figure 2 (a) shows the distribution of T_{ex} of all, and (b) shows the distribution of T_{ex} of each stage. It can be seen from the figure 2 (b) that the excitation temperatures in the protostellar stage are significantly higher than those in the prestellar stage, and their median values are 17.1 K and 7.8 K respectively. It may because of the fact that in the prestellar stage, it is too early to release enough gravitational energy to heat the surrounding environment. However, this trend should be interpreted with caution due to the small number of samples.

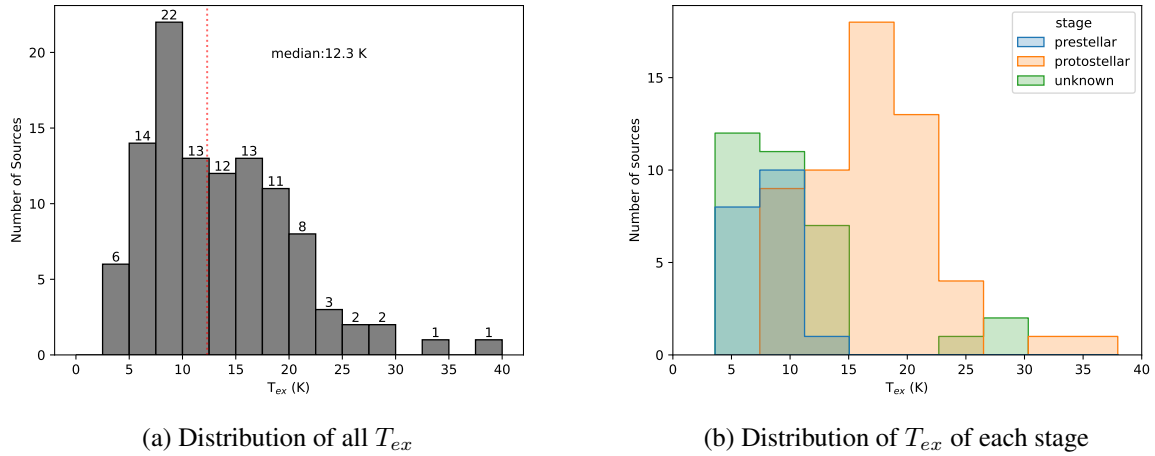
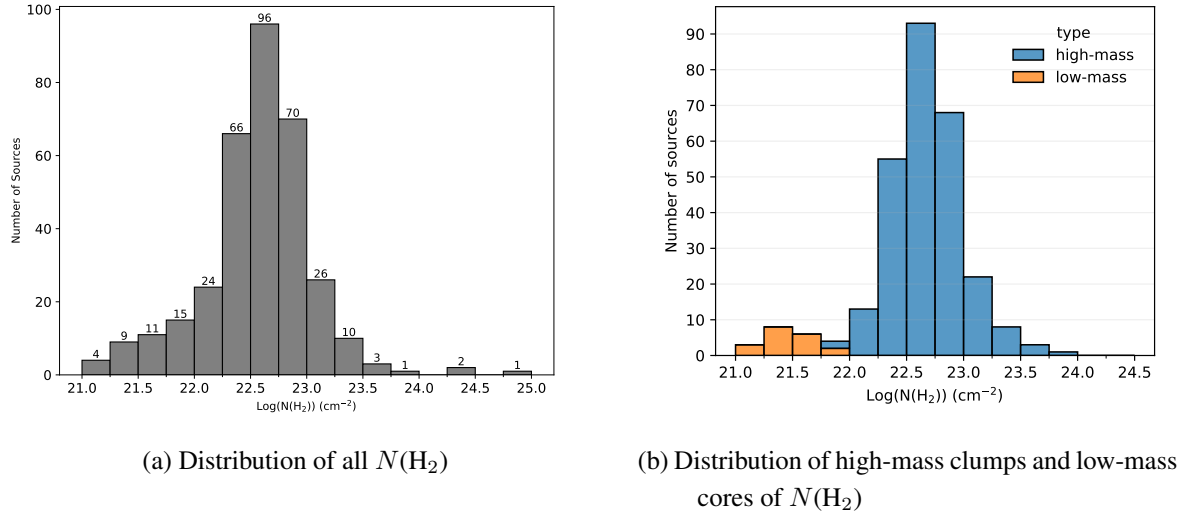
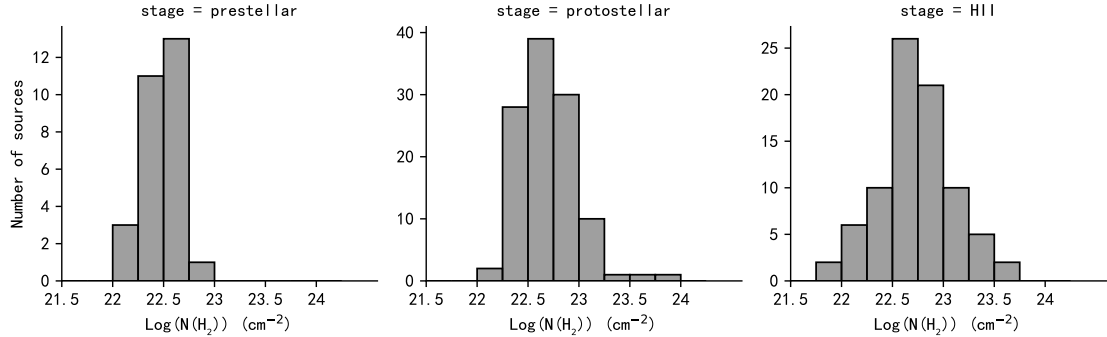


Fig. 2: Distribution of T_{ex}

3.3 Column Density

Figure 3 (a) shows the H_2 column density N_{H_2} distribution of all sources with valid values given in the literature. The column density of H_2 ranges from 1.2×10^{21} to $9.8 \times 10^{24} \text{ cm}^{-2}$, with a median value of $4.17 \times 10^{22} \text{ cm}^{-2}$. Figure 3 (a) shows that N_{H_2} is not log-normally distributed. Figure 3 (b) gives the column density distributions of low-mass and high-mass sources. It can be seen that the N_{H_2} distribution of low-mass cores and high-mass clumps is significantly separated. Their median values are 2.6×10^{21} and $4.8 \times 10^{22} \text{ cm}^{-2}$, respectively. Among them, there are few samples of low-mass cores, so its distribution has little significance. For high-mass clumps, the distribution has a threshold of $10^{22} \sim 10^{24} \text{ cm}^{-2}$, which is consistent with the literature (Rygl et al. 2013; He et al. 2016). Figure 4 presents the distribution of N_{H_2} for high-mass clumps at different evolutionary stages. The median values for high-mass are 3.1×10^{22} , 4.7×10^{22} , $5.4 \times 10^{22} \text{ cm}^{-2}$ for prestellar, protostellar, HII, respectively. Taking into account that the corresponding RMS are 0.18, 0.28, 0.35 in the case of logarithm, respectively, the

Fig. 3: Distribution of H_2 column densityFig. 4: Distribution of H_2 column density for high-mass clumps at different evolutionary stages.

column density of H_2 increases slightly with the evolutionary stage. Different methods for calculating column density are used in different papers, the results of column density calculated using different molecular lines are different based on abundance ratios to hydrogen molecules.

3.4 The Skewness Parameter

As stated in the introduction, the infall motion is signatured by the spectral line asymmetry of optically thick line and a single-peaked profile (Leung & Brown 1977; Zhou 1992; Mardones et al. 1997; Lee et al. 1999; Evans 1999). To demonstrate the measure of asymmetry, Mardones et al. (1997) defined a non-dimensional parameter δV

$$\delta V = \frac{V_{\text{thick}} - V_{\text{thin}}}{\Delta V_{\text{thin}}} \quad (1)$$

where V_{thick} and V_{thin} are the velocities of the peaks of optically thick and thin lines. ΔV_{thin} is the line width (FWHM) of the optically thin line. The values δV obtained from different line pairs may be different. When $\delta V \leq -0.25$ or $\delta V \geq 0.25$, it can usually be considered that the source has a significant blue or red profile.

Different molecules may give different result in studying infall. Mardones et al. (1997) observed 47 protostars to identify infall sources with H_2CO ($2_{12} - 1_{11}$) and CS ($2-1$), and found that the fraction of blue profiles decrease from Class 0 to Class I. However Gregeresen (1998) observed a larger sample which

includes the Class I sources of Mardones et al. (1997), but did not find such trend using $\text{HCO}^+(3-2)$. Fuller et al. (2005) observed $\text{HCO}^+ J = 1 - 0, J = 3 - 2, J = 4 - 3$, and $\text{H}_2\text{CO} (2_{12} - 1_{11})$ toward 77 850 μm continuum sources, and suggests $\text{HCO}^+(1-0)$ and $\text{H}_2\text{CO} (2_{12} - 1_{11})$ trace infall more effectively than $\text{HCO}^+(3-2)$ and $\text{HCO}^+(4-3)$. Rygl et al. (2013) used $\text{HCO}^+(1-0)$, $\text{HCO}^+(4-3)$ and $\text{CO} (3-2)$ to observe another sample of high infrared extinction clouds, came to a similar conclusion. Therefore, the δV values derived from $\text{HCO}^+(1-0)$ and $\text{H}_2\text{CO} (2_{12} - 1_{11})$ are given with high priority.

Figure 5 shows the distribution of 429 valid δV values of all sources. Although δV s are calculated from different lines, we believe this distribution has its scientific significance since the large proportion is identified with $\text{HCO}^+(1-0)$. The median value of δV for all sources is -0.52. For high-mass clumps, the median value identified with $\text{HCO}^+(1-0)$ is -0.50. In contrast, Rygl et al. (2013) derived -0.64 with the same line. For low-mass cores, figure 6 presents the δV distribution of different evolutionary stages. The median values at stages of prestellar and protostellar are -0.46 and -0.74, respectively. Considering the corresponding RMS are 0.16 and 0.33 respectively, the blue asymmetry may have no difference with evolution of low-mass cores. Further observations are needed because of the small sample size. As figure 7 shows, the δV of high-mass infall clumps are -0.55, -0.52, -0.47 at the stage of prestellar, protostellar and HII region respectively. The RMS are 0.23, 0.29, 0.25, respectively. It seems that the blue asymmetry of high-mass infall clumps have the same trend as those of low-mass.

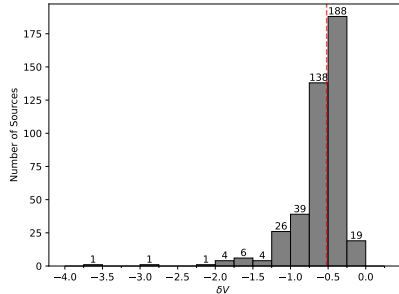


Fig. 5: Distribution of δV for all sources given in the literature. The red dotted line represents the median value of δV .

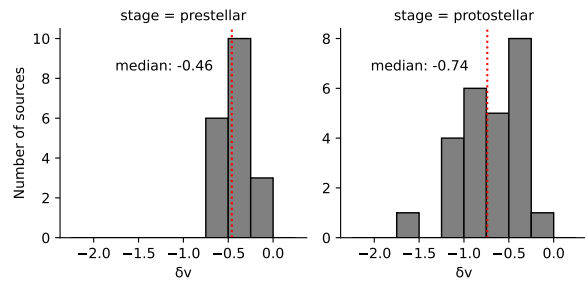


Fig. 6: Distribution of δV for low-mass cores. The red dotted line represents the median value of δV for each stage.

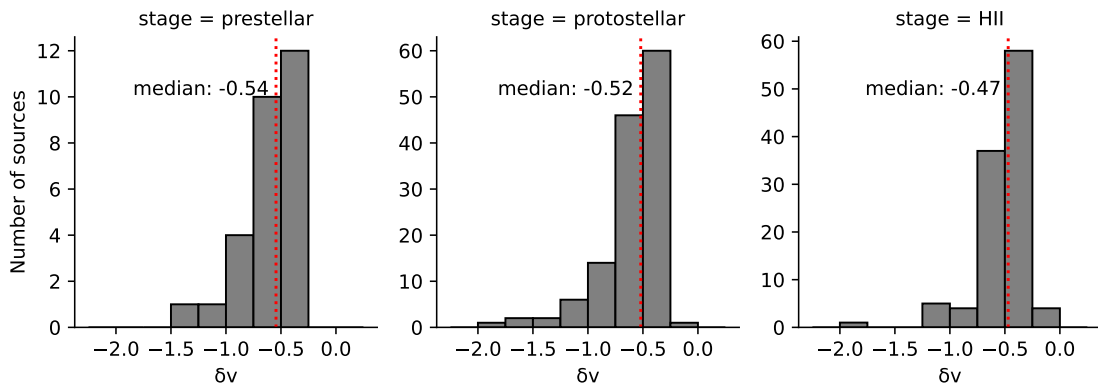


Fig. 7: Distribution of δV for high-mass clumps. The red dotted line represents the median value of δV for each stage.

3.5 Infall Velocity

So far, there are several different approaches to estimate the infall velocity: velocity difference, “two-layer” model, “hill” model, RATRAN, etc. (i) Some works (e.g., Liu et al. 2013; He et al. 2015, 2016; Su et al. 2019) estimated roughly with $V_{\text{in}} = V_{\text{obs}} - V_{\text{sys}}$, where V_{obs} means the velocity at blue peak of the optically thick line, V_{sys} is the system velocity from Gaussian fit of the optically thin line. (ii) The “two-layer” model (Myers et al. 1996) assumes that the excitation temperature in each layer is constant. Some works (e.g., Lee et al. 2001; Qin et al. 2016; Tang et al. 2019; Yue et al. 2021) used the “two-layer” model to calculate the infall velocity with the following equation when $V_{\text{in}} \ll \sigma(2 \ln \tau_0)^{1/2}$,

$$V_{\text{in}} = \frac{\sigma^2}{V_{\text{red}} - V_{\text{blue}}} \ln \left(\frac{1 + e^{(T_{\text{blue}} - T_{\text{dip}})/T_{\text{dip}}}}{1 + e^{(T_{\text{red}} - T_{\text{dip}})/T_{\text{dip}}}} \right) \quad (2)$$

where V_{blue} and V_{red} are the velocities of the blue and red peaks of optically thick line, T_{blue} and T_{red} are the corresponding peak intensities, T_{dip} is the intensity of self-absorption dip between the two peaks, and σ is the velocity dispersion of optically thin line. (iii) The “hill” model assumes that the excitation temperature is increase inward as a linear function of optical depth (De Vries & Myers 2005). De Vries & Myers (2005) thought that the “two-layer” model underestimates the infall velocity by a factor of ~ 2 when matching the two-peak profiles while “hill” model matches better with an rms error of 0.01 km s⁻¹. Blue-asymmetric line profiles with shoulder or redshifted peak can not generally well fitted by the “two-layer” or “hill” model. (iv) A more complex model is RATRAN, which uses 1D Monte Carlo radiative transfer code (Hogerheijde & Van Der Tak 2000) to construct the infall model with more input parameters, such as the radius, mass, density profile, turbulent velocity, kinetic temperature distribution, and the abundance of the molecule. This model can better constrain infall velocity than “two-layer” model (Peretto et al. 2013). The infall velocities derived by different approaches are relatively uniform and will not have a significant impact on the statistical results.

Figure 8 shows the distribution of infall velocities for 354 sources provided in the literature. We give the fitting of lognormal distribution (blue dashed line). The parameters are marked in the upper right of the figure. Kolmogorov–Smirnov (KS) test shows the p value is 0.31. The median value (red dotted line) is 0.97 km s⁻¹. The infall velocity varies with tracers and position across each core (Keown et al. 2016). Liu et al. (2013) believes that infall velocity may be related to the stage of evolution. In order to further study this, we conduct research according to different type of mass and stages. Figure 9 shows the distribution of infall velocity to different evolutionary stages of low-mass cores. The V_{in} of almost all low-mass sources are less than 0.5 km s⁻¹. This is rather different from the result of Liu et al. (2013), which shows the typical infall velocities in low-mass star-forming regions are ~ 0.5 km s⁻¹. The median values of prestellar and protostellar stage are $0.05 (\pm 0.04)$ and $0.17 (\pm 0.20)$ km s⁻¹, suggest that V_{in} may not change with evolution for low-mass cores. However, this result should be interpreted with caution and await further investigation. KS test assumes that the distribution of these two stages is consistent, and the P value is 0.013, rejecting the original hypothesis.

Figure 10 shows the distribution of infall velocities for high-mass clumps at different stages. The median values of prestellar, protostellar and HII region are $1.08 (\pm 0.49)$, $1.14 (\pm 0.62)$ and $1.07 (\pm 1.11)$ km s⁻¹, respectively, implying that the infall velocities of the high-mass clumps have a similar trend to that of the low-mass cores, that is, it may not change with evolutionary stages. It can be seen from the figure that the distributions of these three stages are roughly the same. To confirm this, we performed the KS test, assuming the same distribution. The P value for the first two stages is 0.72, and for the stage of protostellar and HII is P = 0.59, which show that the original hypothesis is not rejected. Skewness is a metrics of the distribution and extent of statistical data, defined as $\text{skew}(X) = E \left[\left(\frac{X - \mu}{\sigma} \right)^3 \right]$, which can

characterize distribution asymmetry. The skewness of the three stages of the massive infall clumps are 1.10, 1.10, 2.10, respectively, which indicates that the distribution of V_{in} tends to be symmetrical at the first two evolutionary stages, while it tends to be rightwing at the HII region stage.

We have also analyzed the influence of different spectral lines on the infall velocity of the sources. The lines adopted by at least 15 sources are used for the following statistics. They are: $\text{HCO}^+(1-0)$, CO (4-3), CS (2-1). For the cores with valid V_{in} values, only CS (2-1) meets the statistical requirement. The median value is $0.05 (\pm 0.04) \text{ km s}^{-1}$, which is basically consistent with the median value 0.07 km s^{-1} of all low-mass cores. This result may change as the sample number of low-mass cores increases. For high-mass clumps, The median values estimated by $\text{HCO}^+(1-0)$ and CO (4-3) are $1.03 (\pm 0.85)$, $3.21 (\pm 1.45) \text{ km s}^{-1}$, respectively. The number of V_{in} estimated by $\text{HCO}^+(1-0)$ accounts for more than 90%, and is thus close to the median value 1.06 of all the high-mass clumps. The sources using CO (4-3) to derive V_{in} are all from [Yue et al. \(2021\)](#).

On the other hand, [Rygl et al. \(2013\)](#) calculated the source (G014.63-00.57 MM1) and showed that the V_{in} derived from $\text{HCO}^+(1-0)$ is about twice as large as that derived from $\text{HCO}^+(4-3)$, but he thought the value derived from $\text{HCO}^+(1-0)$ was overestimated. [Saral et al. \(2018\)](#) used two lines (HCO^+ and HNC) to estimate infall velocities of the same three sources, the results were similar taking into account the error. [Tang et al. \(2019\)](#) estimated V_{in} of one source (G192.16-3.84) with C^{18}O (2-1) and $\text{HCO}^+(3-2)$, indicating that the result derived from $\text{HCO}^+(3-2)$ are slightly larger than C^{18}O (2-1). It can be seen that, due to the lack of total samples, we are temporarily unable to systematically study the influence of different spectral lines on the infall velocity.

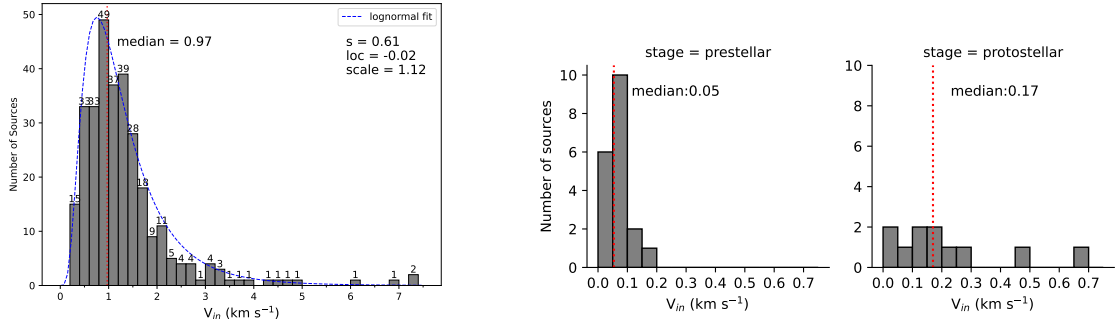


Fig. 8: Distribution of infall velocity. The red dotted line indicates the median value. The blue dashed line is the fitting of lognormal. Fig. 9: Distribution of infall velocity at different evolutionary stages for low-mass cores. The red dotted line represents the median value for each stage.

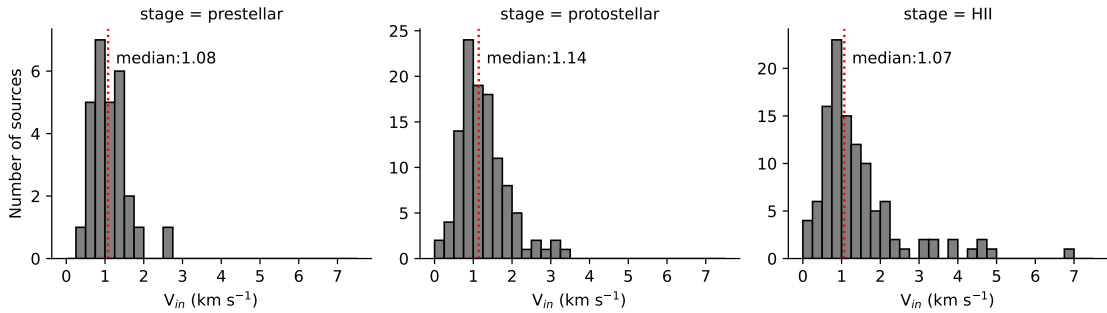


Fig. 10: Distribution of infall velocity for high-mass clumps at different evolutionary stages. The red dotted line represents the median value of V_{in} for each stage.

3.6 Mass Infall Rate

The mass infall rate can be estimated by

$$\dot{M}_{\text{in}} = 4\pi R^2 \mu m_{\text{H}} n_{\text{H}_2} V_{\text{in}} \quad (3)$$

where $\mu = 2.8$ (Wang et al. 2014) is the mean molecular weight, m_{H} is the mass of the hydrogen atom, R is the radius of source (here the source is assumed to be spherical), V_{in} is the infall velocity, n_{H_2} is the mean volume density, which has a conversion relationship with the column density N_{H_2} :

$$n_{\text{H}_2} = \frac{3N_{\text{H}_2}}{R} \quad (4)$$

Figure 11 shows the distribution of mass infall rate of the sources provided in the literature. We could see from the figure that the distribution can be divided into two part, this separation comes from the different type of mass. Among them, we do not know the distribution of low-mass cores because of fewer samples, but for high-mass clumps, it presents an evident lognormal distribution with the P value of 0.82 of KS test. The range of mass infall rate for low-mass cores are $10^{-7} - 10^{-4} \text{ M}_{\odot} \text{yr}^{-1}$, and almost all high-mass clumps are $10^{-4} - 10^{-1} \text{ M}_{\odot} \text{yr}^{-1}$ with only one exception. This is consistent to previous work in high-mass star-forming regions range between $10^{-4} - 10^{-2} \text{ M}_{\odot} \text{yr}^{-1}$ (e.g., Wu et al. 2009; Liu et al. 2013; Qiu et al. 2012; Qin et al. 2016), which are far larger than that of low-mass sources (Beuther et al. 2005; Padoan et al. 2014; Kim et al. 2021).

Padoan et al. (2014) proposed that in most cases, the \dot{M}_{in} is initially the order of $10^{-5} \text{ M}_{\odot} \text{yr}^{-1}$, and may decay rapidly when forming low-mass stars, or maintain relatively large when forming massive stars. Yue et al. (2021) concluded that mass infall rate is independent of the evolutionary stage. Figure 12 shows the distribution of mass infall rate for sources at different evolutionary stages. The orange represents low-mass cores and the blue represents high-mass clumps. The median values of \dot{M}_{in} at each stage for low-mass cores are $6.03 (\pm 0.41) \times 10^{-6}$ and $6.46 (\pm 0.77) \times 10^{-6} \text{ M}_{\odot} \text{yr}^{-1}$ respectively, and for high-mass clumps are $2.63 (\pm 0.46) \times 10^{-3}$, $6.76 (\pm 0.41) \times 10^{-3}$, $7.24 (\pm 0.61) \times 10^{-3} \text{ M}_{\odot} \text{yr}^{-1}$ respectively. Each of them is in the same order of magnitude. We do not find that the mass infall rates of either high-mass or low-mass sources change significantly with evolutionary stages. Note that due to the small number of samples, especially low-mass samples, we need more research to discuss the trend. In addition, the error of distance may also have some influence on the statistical results.

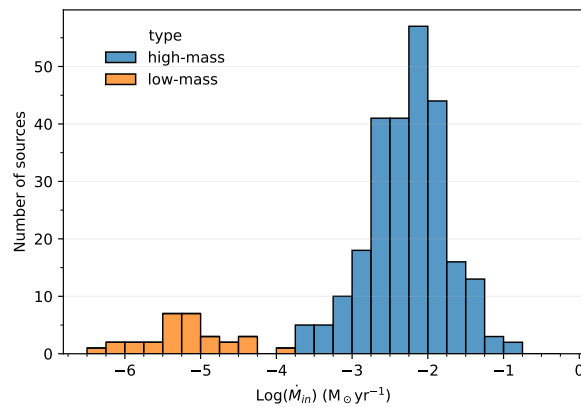


Fig. 11: Distribution of mass infall rate provided in the literature.

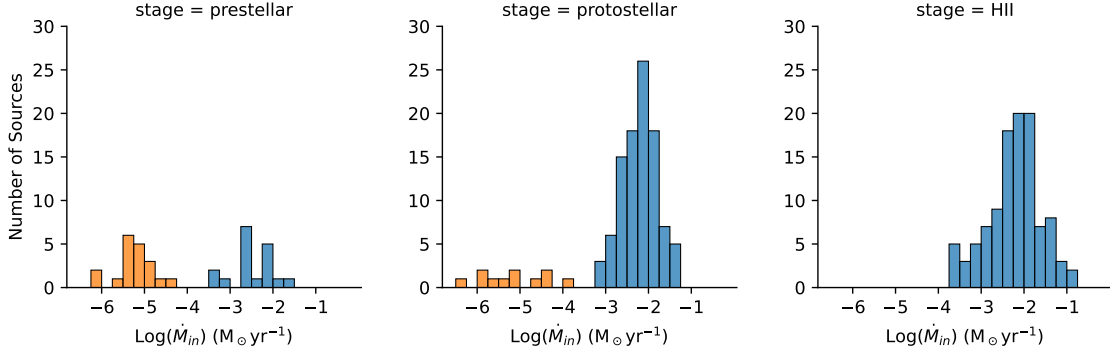


Fig. 12: Distribution of mass infall rate for sources at different evolutionary stages. Orange represents low-mass cores and blue represents high-mass clumps.

3.7 Association with Masers and Outflows

Infall motion is a part of the initial activity of star formation, and maser is also a common phenomenon in star-forming regions. Class I CH₃OH masers are usually associated with outflow because of the collisional pumping mechanism, while class II CH₃OH masers generally occur in compact regions and possibly associated with massive star-forming regions due to the mechanism of radiative pumping. In order to study the correlation, we matched the summarized infall sources with the existing maser database (<https://maserdb.net>).

If a master source is found within 1' of the infall source, we think that they are associated. Table 4 give the association rate between sources and masers with different type of mass. There are 208 sources being associated with masers, the association rate is 46%, and the number for high-mass and low-mass sources are 190 of 352 (54%) and 10 of 54 (19%), respectively. The number associated with masers of Class I CH₃OH, Class II CH₃OH, H₂O, and OH are 130 (29%), 122 (27%), 165 (36%), 75 (16%), respectively. We find that the association rates between high-mass sources and the four kind of masers are generally greater than those of low-mass. This may indicate the star formation activity near massive sources is more intense. In addition, we can see that there's no low-mass sources associate with class II CH₃OH maser, which is consistent with the conclusion that the class II CH₃OH maser is only associated with the massive star-forming region. Of the four masers, the association rate of H₂O is slightly higher, and that of OH is lower for both high-mass and low-mass sources. This may be related to the fact that the samples are not unbiased.

In the early stages of star formation, collapse and infall motion are often accompanied by molecular outflows (Li et al. 2014). The study of the relationship between infall and outflow is helpful to better understand the activity mechanism of star formation. Therefore we also matched these sources with outflows provided in some literature (Wu et al. 2004; Maud et al. 2015; Li et al. 2019; Zhang et al. 2020) in the range of 2'. There are 52 (11%) sources being associated with outflows, which is shown in the appendix table A.1. Part of the reason for the low association rate may be that the outflow samples are incomplete.

4 SUMMARY

We searched the literature related to infall study since 1994, summarized infall sources and made some statistics on the physical properties. The result is summarized below.

1. A total of 456 sources have been cataloged, including 352 (77%) sources with high mass, 55 (12%) with low mass, and the remaining 49 (11%) cannot be categorized. We further divide the high-

Table 4: The maser association rate of sources with different masses.

		CH ₃ OH-I	CH ₃ OH-II	H ₂ O	OH	maser*					
infall sources	high-mass (352)	121	34%	116	33%	151	43%	70	20%	190	54%
	low-mass (54)	7	13%	0	0%	8	15%	2	4%	10	19%
	unknown (50)	2	4%	6	12%	6	12%	3	6%	8	16%
	total (456)	130	29%	122	27%	165	36%	75	16%	208	46%

Notes: * indicates the number of masers detected in any of the four kind of masers.

mass sources into three groups according to the evolutionary stage, that is prestellar, protostellar, HII region. The number in the groups are 48 (11%), 215 (47%), 125 (27%), respectively. The remaining 69 (15%) sources have no evolutionary information. Most of the sources are located within 5 kpc from the sun. We divide the sources into clumps and cores according to their sizes. Vast majority (97%) of the high-mass sources are clumps, and most (85%) of the low-mass sources are cores. Although the current observations are far from complete, the present evidence shows that the star formation activity within the solar circle is more intense than the outer. We summarized the optically thick lines utilized to identify the infall signatures. About 77% of infall sources are identified with HCO⁺ (1-0), suggested this line is more effective in identifying infall sources than the others.

2. The H₂ column densities of high-mass clumps ranges between 10²² and 10²⁴ cm⁻², and those of low-mass cores are about 10²¹ cm⁻². The median value of high-mass clumps is 4.8 × 10²² cm⁻², which is one order of magnitude higher than that of low-mass cores.

3. We counted the skewness of sources and classified them according to different mass and evolutionary stages, but it does not show significant differences with the mass and evolutionary stage.

4. The median value of infall velocities (V_{in}) for high-mass clumps is 1.12 km s⁻¹ with the RMS 1.02, and the V_{in} of nearly all low-mass cores are less than 0.5 km s⁻¹. There is no evidence that infall velocity changes with evolution.

5. The range of mass infall rates for low-mass cores are 10⁻⁷ ∼ 10⁻⁴ M_⊙yr⁻¹, and for high-mass clumps are 10⁻⁴ ∼ 10⁻¹ M_⊙yr⁻¹ with one exception. We do not find that the mass infall rates change with evolutionary stages for either high-mass or low-mass sources.

6. There are 208 (46%) sources associate with masers within an angular radius of 1'. The number of infall sources being associated with masers of Class I CH₃OH, Class II CH₃OH, H₂O, OH are 130 (29%), 122 (27%), 165 (36%), 75 (16%). There are 52 (11%) sources being associated with outflows within 2'.

Acknowledgements This work is supported by the National Key R&D Program of China (grant No. 2017YFA0402702), and the National Natural Science Foundation of China (NSFC, grant Nos. 11873093 and U2031202). Z. Chen acknowledges the support from the NSFC general grant 11903083.

Appendix A: TABLE OF ALL COLLECTED INFALL SOURCES

Table A.1: An Excerpt of the Physical Properties of Infall Sources.

No.	R.A. (J2000)	Dec. (J2000)	Alias	Dist. (kpc)	V_{LSR} (km s $^{-1}$)	$N(\text{H}_2)$ (cm $^{-2}$)	Mass (M $_{\odot}$)	Lines	δv	V_{in} (km s $^{-1}$)	\dot{M}_{in} (M $_{\odot}$ yr $^{-1}$)	Type	Stage	Maser	Outflow	Ref.	
(1)	(2)	(3)	(4)	(5)	(6)	(7)	(8)	(9)	(10)	(11)	(12)	(13)	(14)	(15)	(16)	(17)	(18)
1	00:35:40.1	+66:14:23	Gl21.34+3.42	0.7	-5.3	9.8E+21		1,9	-0.47								3
2	00:36:47.5	+63:29:01	Gl21.30+0.66	1.69	-17.6			2	-0.54								19
3	00:36:53.6	+63:28:03	Gl21.31+0.64	1.7	-17.3	1.7E+22		1,9	-0.63	0.29	1.6E-3						3
4	00:52:25.1	+56:33:54	Gl23.07-6.31	2.53	-30.4			1,2,10	-0.20								19,20
5	02:19:51.8	+61:03:26	Gl33.42+0.00	1.46	-15.2	4.8E+21		9	-0.59								3
6	02:27:03.8	+61:52:25	W3(OH)	1.96	-48.0	6.0E+6		1,10	-0.23	0.06	3.0E-4						14,15,19,20
†7*	02:27:04.7	+61:52:26	W3(H ₂ O)	1.96	-47.8	2.6E+24	1.0E+8	2,10	-0.65	2.70	2.3E-3						9
†8	02:53:12.2	+68:55:52	LDN 1355	0.55	-3.8	1.4E+21	9.1E+3	11	-0.42	0.12	8.4E-6	low	1				6,24
†9	03:26:37.0	+30:15:26	IRAS03235+3004	0.25	4.9			2	-0.66			low	2				25
†10	03:28:32.5	+31:11:05	J03283258+3111040	0.24	7.2			9	-0.45	0.17	6.5E-6	low	2				26
†11	03:28:44.5	+31:05:40	IRAS03256+3055	0.24	7.4			11	-0.31			low	2				22
†12*	03:29:10.5	+31:13:32	NGC 1333-4A	0.24	7.0		1.1E+0	2,3,8,11,12	-0.39	0.68	1.1E-4	low	2				22,23,30
†13*	03:29:12.0	+31:13:09	NGC 1333-4B	0.24	7.1		4.8E-1	2,3,8,11,12	-0.34	0.47	4.0E-5	low	2				22,23,30
†14	03:30:32.6	+30:26:26	J0330326+302626	0.25	6.1			9	-1.11	0.06	3.1E-6	low	2				26
†15	03:33:54.9	+58:08:19	G143.04+1.76	0.51	-8.8	9.6E+21		1,9	-0.34								3
†16	04:10:51.5	+25:09:58	LDN 1498	0.23	7.8	2.8E+21	1.8E+4	11	-0.60	0.03	9.0E-7	low	1				6,24
†17	04:18:40.2	+28:29:25	J0418402+282925	0.23	7.3			9	-0.59	0.03	3.5E-7	low	2				26
†18	04:18:41.8	+28:23:50	LDN 1495A-S	0.23	7.4	2.2E+21	2.8E+4	11	-0.53	0.07	1.0E-5	low	1				6,24
†19	04:19:40.7	+27:13:11	IRAS04166+2706	0.23	6.4			2	-0.97			low	2				25
†20	04:28:38.9	+26:51:35	LDN 1521F	0.23	6.5			2,9	-1.12	0.03	1.7E-6	low	2				26,31
†21	04:30:14.9	+36:00:08	J0430149+360008	0.28	-0.8			9	-0.77	0.12	1.1E-6	low	2				26
†22	04:32:48.7	+24:25:12	TMC2	0.23	6.4	4.5E+21	2.3E+4	11	-0.23	0.17	4.0E-5	low	1				6,24
†23	04:39:35.0	+25:41:47	TMC-1A	0.23	6.0			2	-1.02			low	2				25
†24	04:39:53.6	+26:03:06	LDN 1527	0.23	5.9		2,3,12	-0.99			low	2				22	
†25	04:41:33.0	+25:44:44	TMC1	0.23	5.8	6.9E+21	6.3E+3	11	-0.53	0.05	6.0E-6	low	1				6,24
†26	04:47:13.1	+53:03:57	G154.05+5.08	0.26	4.3	3.1E+21		1	-1.91								3
†27	05:04:14.9	+25:11:08	LDN 1544	0.23	7.2	8.0E+21	1.4E+4	11	-0.36	0.02	9.0E-7	low	1				6,24
†28	05:17:36.0	+25:05:18	LDN 1552	0.23	7.8	3.8E+21	2.3E+4	11	-0.46	0.12	8.1E-6	low	1				6,24
29	05:35:50.9	+36:10:41	G172.77+2.09	1.69	-15.3	6.0E+21		1	-0.62	0.04		low	2				3
30	05:41:00.0	+35:48:04	SH 2-235N	1.68	-19.6			1	-0.43			high	2				20
31	05:52:12.1	+26:59:35	IRAS05490+2658	4.42	0.8			1	-0.53			high	2	3	Y	27	

Table A.1: An Excerpt of the Physical Properties of Infall Sources.

No.	R.A. (J2000)	Dec. (J2000)	Alias	Dist. (kpc)	V_{LSR} (km s $^{-1}$)	$N(\text{H}_2)$ (cm $^{-2}$)	Mass (M $_{\odot}$)	Lines	δv	V_{in} (km s $^{-1}$)	\dot{M}_{in} (M $_{\odot}$ yr $^{-1}$)	Type	Stage	Maser	Outflow	Ref.		
(1)	(2)	(3)	(4)	(5)	(6)	(7)	(8)	(9)	(10)	(11)	(12)	(13)	(14)	(15)	(16)	(17)	(18)	
†32	05:54:38.8	+01:53:44	LDN 1622A-2	0.42	1.2	5.1E+21	3.0E+3		11	-0.11	0.09	1.2E-5	low	1			6,24	
†33*	05:58:13.5	+16:31:58	G192.16-3.84	1.55	6.0	2.7E+24		10.8(4.8)	2,14	-0.10	2.00	4.7E-3	high	2	3	Y	7	
34	06:07:41.5	+20:39:44	G189.67+0.17	2.1	7.3	2.5E+22			1				high	3	13	Y	14,18	
35	06:10:51.0	-06:11:50	G213.88-11.84	0.84	10.0				1			0.80	high	3	123	Y	14,15	
36	06:12:53.6	+17:59:27	J06125362+1759279	1.69	9.0		4.0E+5		1			0.90	2.0E-4	high	3	123	Y	14,15
37	06:12:53.6	+18:00:26	G192.5840-00.0411	1.69	9.0		9.8E+24	6.6E+9	1.64	16		2.50	2.3E-4	high	2	123	Y	4
†38*	06:12:54.0	+17:59:23	SH 2-255IR SMA1	1.67					9	-0.17		6.0E-4		2		Y	3	
39	06:14:25.2	+17:43:20	G193.01+0.14	1.68	7.9	1.7E+22			1	-0.25		5.1E-3		2	3	Y	3	
40	06:59:14.3	-03:54:35	G217.30-0.05	2.56	26.6	2.6E+22			1				high	3	34	Y	14,15	
41	07:44:51.9	-24:07:40	IRAS 07427-2400	5.06	68.0				1				high	3	123	Y	1	
42	09:03:32.8	-48:28:10	IRAS0918-4816	3.8	10.4		3.9E+5	1.0E+3	6	-0.61	3.41	4.8E-2	high	3	123			
43	12:27:36.5	-62:51:26	G300.218-0.111	4.13	-40.0	3.9E+22	1.1E+4	7.4E+2	1,7	-0.31	0.51	1.9E-3	high	2			12	
44	12:43:31.0	-62:36:24	G302.021+0.251	4.32	-46.0	4.5E+22	1.8E+4	6.9E+2	1	-0.42	1.23	5.0E-3	high	3	3		12	
45	12:54:16.0	-61:37:23	G303.268+1.247	1.8	-30.4	1.9E+22	6.7E+3	1.0E+3	1	-0.41	0.51	1.9E-3	high	3			12	
46	13:05:39.1	-62:14:39	G304.586+0.582	1.74	-22.3	1.7E+22	3.0E+5	4.3E+1	1	-0.29	0.41	6.7E-4	high	3			12	
47	13:06:33.2	-62:33:49	G304.672+0.257	3.5	-43.2	2.8E+22		3.2E+2	1,7	-0.65	1.25	high	2				12	
†48	13:07:36.1	-77:00:05	BHR 86	0.15	3.8				11,12	-0.40			low	2	2		22	
49	13:08:11.6	-62:10:20	G304.886+0.636	2.82	-36.3	4.8E+22	7.8E+4	3.0E+2	1	-0.38	0.44	1.7E-3	high	2	23		12	
50	13:16:43.1	-62:58:30	IRAS13134-6242	4.14	-32.2		2.8E+4	1.3E+3	6	-0.31	1.99	1.4E-2	high	3	123	Y	1	
51	13:16:48.4	-62:50:36	G305.822-0.114	3.62	-41.5	5.8E+22	2.9E+4	8.3E+2	1,7	-0.54	1.30	7.1E-3	high	2			12	
52	13:39:54.3	-61:41:09	G308.646+0.647	3.72	-46.6	4.2E+22	6.9E+3	6.6E+2	1	-0.65	1.44	4.2E-3	high	3	3		12	
53	13:40:54.0	-61:46:49	G308.744+0.532	3.23	-47.0	2.1E+22	9.5E+3	2.8E+3	1	-0.26	0.54	4.6E-3	high	3			12	
54	13:41:53.0	-62:07:32	G308.791+0.171	5.01	-50.5	1.9E+22	1.4E+4	9.3E+2	1	-0.69	0.90	4.2E-3	high	3			12	
55	13:43:01.4	-62:08:56	G308.917+0.122	5.01	-50.0	3.8E+22	4.2E+3	1.6E+3	1	-0.28	0.94	4.2E-3	high	3			12	
56	13:45:51.1	-62:33:42	G309.154-0.349	4.44	-40.9	2.5E+22	4.4E+4	5.8E+2	1,7	-0.48	1.24	6.1E-3	high	2			12	
57	13:48:37.9	-62:46:12	G309.421-0.621	2.7	-42.5	7.2E+22	1.1E+4	1.4E+3	1,7	-0.48	0.94	5.3E-3	high	3			12	
58	13:50:55.0	-61:44:21	G309.911+0.324	4.59	-59.4	9.5E+22	1.4E+4	3.2E+3	1,7	-0.39	0.84	8.9E-3	high	2	13		12	
59	13:51:03.7	-61:30:25	G309.981+0.546	2.56	-40.9	3.9E+22	2.7E+4	4.8E+2	1,7	-1.90	1.33	4.9E-3	high	3			12	
60	13:51:13.1	-61:32:34	G309.991+0.507	2.56	-41.0	2.5E+22	8.7E+4	4.3E+2	1,7	-0.47	0.60	3.0E-3	high	2			12	
61	13:51:38.4	-61:39:15	G310.014+0.387	4.41	-41.1	8.1E+22	1.3E+4	9.1E+2	1	-0.31	0.62	2.8E-3	high	3			12	
62	13:56:01.1	-62:14:20	G310.374-0.304	4.4	-52.6	5.9E+22	1.5E+4	1.8E+3	1	-0.26	0.59	4.3E-3	high	2	1		12	

Table A.1: An Excerpt of the Physical Properties of Infall Sources.

No.	R.A. (J2000)	Dec. (J2000)	Alias	Dist. (kpc)	V_{LSR} (km s $^{-1}$)	$N(\text{H}_2)$ (cm $^{-2}$)	$n(\text{H}_2)$ (cm $^{-3}$)	Mass (M $_{\odot}$)	Lines	δv	V_{in} (km s $^{-1}$)	\dot{M}_{in} (M $_{\odot}$ yr $^{-1}$)	Type	Stage	Maser	Outflow	Ref.
(1)	(2)	(3)	(4)	(5)	(6)	(7)	(8)	(9)	(10)	(11)	(12)	(13)	(14)	(15)	(16)	(17)	(18)
63	14:03:34.4	-61:15:47	G311.492+0.404	4.36	-58.6	2.6E+22	5.8E+4	6.9E+2	1	-0.52	1.01	6.1E-3	high	3			12
64	14:08:42.3	-61:10:43	G312.108+0.309	4.03	-47.9	5.4E+22	8.0E+3	9.8E+2	1,7	-1.06	2.43	9.6E-3	high	3	2		12
65	14:26:04.4	-60:40:54	G314.264+0.091	3.74	-51.3	7.9E+22	9.1E+3	2.0E+3	1,7	-0.37	0.96	6.5E-3	high	3			12
66	14:42:02.7	-60:30:36	G316.139-0.506	3.73	-60.0	6.0E+22	3.7E+3	4.9E+3	1,7	-0.60	1.22	1.1E-2	high	3			12
67	14:42:02.8	-60:30:35	IRAS14382-6017	3.74	-60.2	3.5E+3	4.0E+3	6	-0.60	2.04	1.5E-2	high	3			1	
68	14:42:12.2	-60:41:09	G316.084-0.674	2.34	-38.9	2.8E+22		1.5E+3	1,7	-0.49	1.26	high	2				12
69	14:53:42.8	-59:08:57	IRAS14498-5856	3.38	-49.8	1.0E+4	1.0E+3	6	-0.66	3.77	1.6E-2	high	3			1	
70	15:03:39.5	-57:39:30	G319.899+0.791	2.32	-42.8	2.1E+22	5.8E+3	4.5E+2	1,7	-0.41	0.88	1.9E-3	high	3			12
71	15:05:22.5	-57:27:06	G320.201+0.859	2.34	-41.0	3.4E+22	1.7E+4	6.6E+2	1,7	-0.56	1.07	4.2E-3	high	3			12
72	15:07:21.3	-57:49:28	G320.247+0.404	1.51	-32.7	7.8E+22	7.1E+3	7.8E+2	1	-0.28	0.51	1.7E-3	high	3			12
73	15:11:54.9	-58:09:58	G320.596-0.196	3.3	-52.2	4.7E+22	1.8E+4	3.7E+2	1	-0.43	0.91	2.5E-3	high	3	4		12
74	15:30:57.1	-56:15:03	G323.799+0.017	3.27	-58.3	2.7E+22	1.4E+4	1.4E+3	1	-0.64	1.54	9.5E-3	high	2	2		12
75	15:39:10.7	-54:55:43	G325.514+0.414	3.01	-45.8	3.0E+22	1.3E+4	2.6E+3	1,7	-0.49	0.92	8.2E-3	high	3			12
†76	15:43:01.4	-34:09:12	B228	0.15	5.4				2	-0.74		low	2				25
77	15:43:33.2	-53:55:28	G326.626+0.834	2.92	-38.0	6.3E+22	2.9E+4	5.1E+2	1	-0.30	0.62	2.4E-3	high	2			12
78	15:46:21.1	-54:10:42	G326.796+0.382	1.27	-20.7	6.6E+22	3.0E+4	1.6E+2	1	-0.57	0.84	1.6E-3	high	2			12
79	15:49:08.2	-54:23:07	G326.987-00.031	3.17	-58.2	2.6E+3	1.0E+3	1,7	-0.53	1.80	4.9E-3	high	2			28	
80	15:50:19.0	-53:57:05	G327.393+0.199	6.05	-89.1	1.0E+23	1.2E+4	2.3E+3	1	-0.27	0.79	6.3E-3	high	2	123		12
†81	15:54:01.1	+02:34:47	LDN 183	0.22	2.6	4.4E+21	2.7E+4	11	-0.06	0.05	9.8E-6	low	1			6,24	
82	15:55:48.8	-52:43:06	IRAS15520-5234	2.88	-41.7	2.2E+4	1.6E+3	6	-0.46	4.33	3.1E-2	high	3	1234		1	
83	15:56:01.7	-53:09:45	G328.549+0.271	3.16	-58.8	3.2E+22	4.2E+4	3.2E+2	1,7	-0.42	0.94	3.0E-3	high	2	1		12
84	15:56:35.7	-54:14:41	G327.918-0.612	2.93	-45.8	3.8E+22	6.6E+4	1.9E+2	1,7	-0.58	0.96	2.6E-3	high	2			12
85	15:58:07.5	-51:43:25	G329.721+1.165	5.03	-77.3	5.6E+22	2.3E+4	1.2E+3	1	-0.33	0.97	6.1E-3	high	2			12
86	16:00:32.0	-53:12:54	G329.029-00.206	2.89	-43.5	1.4E+3	2.8E+3	1,7	-0.64	2.34	8.0E-3	high	2			28	
87	16:01:33.8	-53:11:13	G329.164-0.286	2.97	-50.0	5.6E+22	1.2E+4	4.4E+3	1,7	-0.52	1.04	1.3E-2	high	2	12		12
88	16:01:45.2	-52:40:18	G329.524+0.084	5.44	-88.6	5.2E+22	5.0E+3	3.3E+3	1	-0.28	0.93	7.1E-3	high	3	3		12
89	16:02:22.7	-53:06:06	G329.312-0.302	4.51	-73.9	4.4E+22	2.4E+4	8.7E+2	1	-0.35	0.64	3.4E-3	high	2			12
90	16:03:32.3	-53:09:28	IRAS15596-5301	4.85	-74.2	5.5E+3	8.0E+3	6	-0.61	3.33	4.5E-2	high	3	234		1	
91	16:09:52.9	-51:54:55	IRAS16060-5146	5.1	-90.4	1.7E+4	8.0E+3	6	-0.56	3.91	7.7E-2	high	3	1234		1	
92	16:09:58.0	-50:56:20	G331.626+0.526	2.96	-51.4	5.1E+22	8.9E+3	8.1E+2	1,7	-0.34	0.70	2.5E-3	high	3	1		12
93	16:10:01.6	-50:49:37	G331.709+0.602	4.61	-67.5	1.2E+23	1.4E+4	2.9E+3	1,7	-0.40	1.39	1.4E-2	high	2	12		12

Table A.1: An Excerpt of the Physical Properties of Infall Sources.

No.	R.A. (J2000)	Dec. (J2000)	Alias	Dist. (kpc)	V_{LSR} (km s $^{-1}$)	$N(\text{H}_2)$ (cm $^{-2}$)	$n(\text{H}_2)$ (cm $^{-3}$)	Mass (M $_{\odot}$)	Lines	δv	V_{in} (km s $^{-1}$)	\dot{M}_{in} (M $_{\odot}$ yr $^{-1}$)	Type	Stage	Maser	Outflow	Ref.	
(1)	(2)	(3)	(4)	(5)	(6)	(7)	(8)	(9)	(10)	(11)	(12)	(13)	(14)	(15)	(16)	(17)	(18)	
94	16:10:06.8	-50:50:29	G331.709+0.582	4.56	-66.7	1.2E+23	1.8E+4	1.5E+3	1	-0.80	2.90	2.0E-2	high	2	1	12		
95	16:11:00.0	-51:50:22	IRAS16071-5142	5.05	-86.8	1.2E+4	5.0E+3	6	-0.47	4.59	5.8E-2	high	3	1234		1		
96	16:11:18.3	-52:02:04	G331.034-0.419	4.87	-64.9	7.4E+22	1.3E+4	3.6E+3	1	-0.32	0.97	1.1E-2	high				12	
97	16:11:20.1	-52:02:48	G331.029-0.431	3.91	-64.4	6.5E+22	9.7E+3	3.0E+3	1,7	-0.48	1.45	1.3E-2	high				12	
98	16:11:23.1	-52:01:22	G331.051-0.419	4.85	-65.6	2.8E+22	7.2E+3	1.9E+3	1	-0.31	1.30	7.8E-3	high				12	
99	16:11:27.1	-51:41:57	IRAS16076-5134	5.05	-88.4	4.2E+3	4.0E+3	6	-0.75	6.90	5.4E-2	high	3	1234		1		
†100*	16:11:32.6	-51:34:35	G331.372-00.116	5.05	-87.7	3.0E+23	8.5E+5	1.8E+1	2	-1.54	2.0E-3	high	1				2	
101	16:11:59.3	-51:28:14	G331.496-0.079	5.04	-88.1	4.2E+22	9.8E+4	1.1E+3	1	-0.41	1.08	1.0E-2	high	3	1	1	12	
102	16:12:04.1	-52:00:49	G331.134-0.484	4.15	-68.3	8.5E+22	2.7E+3	6.6E+3	1	-0.26	0.80	7.9E-3	high	3	1	1	12	
103	16:12:05.9	-51:29:10	G331.498-0.102	5.03	-88.0	6.5E+22	1.1E+4	2.3E+3	1	-0.49	1.47	1.2E-2	high	3	134		12	
104	16:12:09.9	-51:28:36	G331.512-0.102	5.03	-88.9	2.2E+23	2.4E+4	4.9E+3	1,7	-0.56	2.20	3.7E-2	high	3	1234		12	
105	16:12:27.0	-51:43:32	G331.374-0.314	5.05	-97.0	2.8E+22			1,7	-0.52	1.10	high	2				12	
106	16:12:60.0	-51:31:43	G331.571-0.229	2.96	-50.3	3.6E+22	1.1E+4	3.2E+2	1,7	-0.30	0.51	1.1E-3	high	2			12	
107	16:15:17.4	-50:55:60	G332.241-0.044	2.91	-47.7	8.7E+22	7.8E+3	1.8E+3	1	-0.65	1.84	1.1E-2	high	2	1	1	12	
108	16:15:24.1	-50:55:59	G332.254-0.056	2.92	-48.3	3.7E+22	3.1E+4	6.9E+2	1,7	-0.48	0.89	4.4E-3	high	2	1	1	12	
109	16:15:34.1	-50:55:43	G332.276-0.071	2.91	-48.0	2.1E+22	1.1E+4	4.7E+2	1,7	-0.99	1.42	3.8E-3	high	2			12	
110	16:15:45.7	-50:55:53	G332.296-0.094	2.93	-49.0	1.5E+23	6.8E+3	1.7E+3	1	-0.67	1.57	8.6E-3	high	3	123		12	
111	16:16:42.9	-50:50:17	G332.469-0.131	2.95	-50.2	2.3E+22	8.1E+3	4.7E+2	1	-0.41	0.54	1.3E-3	high	3			12	
112	16:17:11.6	-50:47:13	G332.559-0.147	2.9	-46.8	2.8E+22	1.7E+4	7.9E+2	1	-0.28	0.44	2.0E-3	high	2	2	2	12	
113	16:17:29.2	-50:46:12	G332.604-0.167	2.9	-46.5	4.6E+22	3.6E+3	1.5E+3	1,7	-0.73	1.78	7.3E-3	high	2	123		12	
114	16:19:48.0	-51:02:18	G332.677-0.614	3.29	-57.7	8.7E+22	6.1E+3	1.1E+4	1,7	-0.46	1.07	1.9E-2	high	3			12	
115	16:20:07.2	-50:04:50	G333.386+0.032	4.76	-70.3	3.9E+22	8.8E+3	3.1E+3	1,7	-0.50	1.27	1.1E-2	high	3	1234		12	
116	16:20:26.4	-50:41:43	G332.990-0.441	3.03	-55.5	8.1E+21	3.6E+3	1.3E+2	1	-0.52	0.34	2.6E-4	high	3	13		12	
117	16:20:29.3	-50:33:44	G333.089-0.352	2.97	-52.5	1.4E+22	3.7E+3	3.0E+2	1	-0.29	0.65	8.9E-4	high	3			12	
118	16:20:34.2	-50:51:19	G332.892-0.569	3.12	-57.0	1.3E+22	1.2E+4	3.8E+2	1	-0.44	0.93	2.2E-3	high	1			12	
119	16:20:43.2	-50:37:04	G333.076-0.417	2.99	-54.4	4.4E+22	2.3E+4	7.6E+2	1,7	-0.29	0.52	2.5E-3	high				12	
120	16:21:20.4	-50:11:17	G333.449-0.182	2.86	-44.2	3.5E+22	3.1E+4	4.7E+2	1,7	-0.45	1.65	6.2E-3	high	1	2	2	12	
121	16:21:21.8	-50:49:46	G332.999-0.639	2.92	-48.0	1.4E+22	4.5E+3	2.3E+2	1,7	-0.80	1.66	2.1E-3	high	2			12	
122	16:22:03.3	-50:11:48	G333.524-0.269	2.93	-49.5	6.0E+22	3.1E+3	2.5E+3	1,7	-0.49	1.10	5.8E-3	high	1	1	1	12	
123	16:22:38.9	-50:01:39	G333.711-0.217	2.9	-47.3	1.5E+22	3.3E+4	1.6E+2	1	-0.61	1.13	2.2E-3	high	2			12	
124	16:23:43.4	-48:52:37	G334.651+0.469	4.55	-65.4	1.9E+22	8.2E+3	8.5E+2	1,7	-0.81	1.08	3.9E-3	high	2			12	

Table A.1: An Excerpt of the Physical Properties of Infall Sources.

No.	R.A. (J2000)	Dec. (J2000)	Alias	Dist. (kpc)	V_{LSR} (km s $^{-1}$)	$N(\text{H}_2)$ (cm $^{-2}$)	$n(\text{H}_2)$ (cm $^{-3}$)	Mass (M $_{\odot}$)	Lines	δv	V_{in} (km s $^{-1}$)	\dot{M}_{in} (M $_{\odot}$ yr $^{-1}$)	Type	Stage	Maser	Outflow	Ref.
(1)	(2)	(3)	(4)	(5)	(6)	(7)	(8)	(9)	(10)	(11)	(12)	(13)	(14)	(15)	(16)	(17)	(18)
†125	16:26:26.4	-24:24:30	VLA 1623	0.16	3.7				11,12	-0.64	0.98	6.2E+2	low	2	3	Y	22
126	16:26:55.4	-48:25:03	G335.349+0.412	4.49	-59.4	2.2E+22	6.7E+4	6.8E+2	1	-0.62	0.98	6.2E-3	high	2			12
†127	16:26:59.0	-24:34:57	WL 22	0.16	3.8				11,12	-0.99			low	2			22
128	16:27:26.8	-49:12:39	G334.838-0.201	2.87	-45.0	2.5E+22	6.7E+3	1.9E+2	1	-0.46	0.65	8.3E-4	high	3			12
129	16:28:51.2	-48:50:41	G335.262-0.114	2.85	-44.1	3.0E+22	2.3E+4	7.6E+2	1,7	-1.27	1.79	8.5E-3	high	2			12
130	16:29:03.6	-48:59:41	G335.177-0.242	2.86	-45.6	1.3E+22	6.5E+3	5.5E+2	1,7	-1.11	0.92	2.3E-3	high	3			12
131	16:30:59.1	-48:43:53	IRAS16272-4837	2.88	-46.6	1.1E+4	1.6E+3	6	-0.40	2.58	1.5E-2	high	3	1234	Y	1	
132	16:30:59.2	-48:43:53	G335.586-0.291	2.89	-46.9	3.4E+23	1.3E+4	3.3E+3	1	-0.27	0.73	7.6E-3	high	3	1234	Y	12
†133	16:31:26.8	+24:15:54	IRAS16293-2422	0.07	4.0				2,3,11,12				low	2			22
†134	16:33:49.1	+24:25:28	LDN 1689B	0.07	4.0	1.8E+21	2.5E+4		11	-0.29	0.05	4.9E-6	low	1			6,24
135	16:34:13.3	-48:06:14	G336.411-0.256	4.49	-87.6	6.5E+22	2.0E+3	5.9E+3	1	-0.30	1.17	9.6E-3	high	3	12		12
136	16:36:17.1	-47:40:44	G336.958-0.224	4.39	-71.6	4.6E+22	3.9E+3	6.3E+3	1,7	-0.56	1.44	1.6E-2	high	2			23
137	16:36:18.8	-47:23:19	G337.176-0.032	4.39	-68.4	7.4E+22	4.4E+3	3.6E+3	1,7	-0.42	1.42	1.1E-2	high	2			23
138	16:36:56.4	-47:22:27	G337.258-0.101	4.38	-68.2	7.4E+22	3.7E+3	1.2E+4	1,7	-0.44	1.38	2.2E-2	high	2			234
139	16:38:29.6	-47:00:41	IRAS16348-4654	2.8	-46.9				7.5E+3	2.5E+4	6	-0.51	1.81	5.8E-2	high	3	1234
140	16:38:51.0	-47:27:58	IRAS16351-4722	2.69	-40.2	2.0E+4	1.6E+3	6	-0.76	3.02	2.1E-2	high	3	1234	1		
141	16:38:58.0	-47:07:41	G337.671-0.192	2.94	-51.6	4.2E+22	1.3E+4	5.0E+2	1	-0.34	0.85	2.5E-3	high	3			12
142	16:39:48.5	-47:12:41	G337.704-0.354	2.72	-41.6	9.3E+21	1.8E+3	4.0E+3	1	-0.45	0.94	5.8E-3	high	3			12
143	16:39:57.9	-47:09:31	G337.761-0.339	2.72	-41.8	9.1E+22	1.3E+4	2.1E+3	1,7	-0.39	1.08	8.3E-3	high	2			12
144	16:39:58.2	-48:02:46	G337.098-0.929	2.67	-41.8	3.5E+22	1.5E+4	3.7E+2	1,7	-0.64	1.28	3.2E-3	high	2			12
145	16:40:13.8	-45:38:30	G338.926+0.634	4.55	-61.8	9.1E+22	4.6E+3	2.1E+3	1,7	-0.88	3.20	1.7E-2	high	2			12
146	16:40:27.1	-47:07:16	G337.844-0.376	2.7	-40.0	5.0E+22	2.8E+3	5.4E+3	1	-0.31	0.50	4.3E-3	high	3	2		12
148	16:40:50.9	-46:27:37	G338.384+0.011	2.57	-38.9	1.7E+22	1.3E+4	3.3E+2	1	-0.46	1.29	2.9E-3	high	2			23
147	16:40:50.9	-46:23:27	G338.436+0.057	2.67	-32.2	7.9E+22	7.1E+3	1.5E+3	1	-0.60	2.45	1.3E-2	high	3			12
149	16:41:01.3	-47:05:46	G337.927-0.432	2.68	-39.1	1.5E+22	1.0E+3	7.1E+2	1	-0.43	1.34	2.1E-3	high	3	2		12
150	16:41:10.6	-47:08:03	G337.916-0.477	2.68	-38.8	3.2E+23	2.0E+4	1.9E+3	1,7	-0.49	1.29	1.1E-2	high	2			1234
151	16:41:16.5	-45:48:57	G338.916+0.382	2.55	-24.5	6.2E+22	3.5E+3	1.6E+4	1	-0.47	1.22	2.4E-2	high	3	23		12
152	16:41:22.7	-47:08:26	G337.934-0.507	2.67	-38.6	6.0E+22	7.0E+3	8.9E+2	1,7	-0.90	2.10	7.5E-3	high	3			12
153	16:42:28.0	-46:46:50	G338.327-0.409	2.66	-38.2	3.2E+22	1.7E+4	2.0E+2	1	-0.65	1.30	2.3E-3	high	2	12		12
154	16:44:14.2	-45:31:27	G339.476+0.184	6.1	-92.1	5.5E+22	4.9E+3	3.6E+3	1,7	-0.62	2.15	1.7E-2	high	3	23		12
155	16:45:05.9	-45:30:19	G339.589+0.082	6.14	-109.7	3.2E+22	2.0E+3	3.5E+3	1,7	-0.57	1.50	8.7E-3	high	3			12

Table A.1: An Excerpt of the Physical Properties of Infall Sources.

No.	R.A. (J2000)	Dec. (J2000)	Alias	Dist. (kpc)	V_{LSR} (km s $^{-1}$)	$N(\text{H}_2)$ (cm $^{-2}$)	$n(\text{H}_2)$ (cm $^{-3}$)	Mass (M $_{\odot}$)	Lines	δv	V_{in} (km s $^{-1}$)	\dot{M}_{in} (M $_{\odot}$ yr $^{-1}$)	Type	Stage	Maser	Outflow	Ref.
(1)	(2)	(3)	(4)	(5)	(6)	(7)	(8)	(9)	(10)	(11)	(12)	(13)	(14)	(15)	(16)	(17)	(18)
156	16:45:59.2	-45:38:43	G339.584-0.127	2.61	-34.1	1.1E+23	3.9E+4	7.4E+2	1	-0.78	2.20	1.2E-2	high	2	123	12	
†157	16:46:51.9	+13:47:60	LDN 158	0.19	4.0	1.5E+21	4.1E+5		11	-0.56	0.07	7.6E-6	low	1			6,24
158	16:47:03.5	-45:21:31	G339.924-0.084	4.2	-53.1	7.8E+22	2.7E+3	1.3E+4	1,7	-0.42	1.19	1.8E-2	high	2	3	12	
†159	16:47:37.9	+10:38:49	LDN 234E-C	0.22	2.9	1.9E+21	2.8E+5		11	-0.55	0.05	3.3E-6	low	1			6,24
†160	16:47:44.3	+10:46:54	LDN 234E-S	0.22	3.1	2.6E+21	3.5E+4		11	-0.63	0.05	4.0E-6	low	1			6,24
161	16:47:56.5	-45:07:15	G340.206-0.049	8.91	-120.9	3.5E+22	5.6E+3	2.1E+3	1,7	-0.50	1.52	8.9E-3	high				12
162	16:48:13.9	-45:21:46	G340.054-0.244	4.31	-53.1	1.9E+23	4.0E+3	3.2E+3	1,7	-0.46	1.38	9.5E-3	high	3	1234		
163	16:48:27.5	-45:09:48	G340.232-0.146	2.92	-50.5	3.1E+22	5.4E+3	9.1E+3	1	-0.62	1.51	2.3E-2	high	2			12
164	16:48:40.9	-45:15:57	G340.179-0.242	4.32	-53.3	2.7E+22	1.9E+3	1.9E+4	1	-0.33	1.12	2.0E-2	high	1			12
165	16:48:46.9	-45:10:24	G340.261-0.196	2.76	-43.8	2.6E+22	5.4E+3	8.9E+2	1	-0.49	1.36	4.4E-3	high				12
166	16:50:14.9	-44:42:32	G340.784-00.097	5.85	-101.4	3.0E+2	3.7E+3		1	-1.14	0.90	3.0E-3	high				28
167	16:50:51.6	-44:08:44	G341.287+0.179	2.51	-23.6	2.4E+22	2.4E+4	3.7E+2	1,7	-0.85	1.53	4.6E-3	high				1234
168	16:50:53.9	-44:09:28	G341.282+0.166	2.52	-24.3	1.4E+22	1.3E+4	1.3E+2	1	-0.69	1.02	1.2E-3	high	2			12
169	16:51:44.9	-44:46:39	G340.901-0.346	2.76	-43.1	2.1E+22	5.3E+4	3.6E+2	1,7	-1.92	3.03	1.2E-2	high	2			12
170	16:52:17.8	-44:26:55	G341.217-0.212	2.75	-43.1	1.0E+23	2.4E+4	6.9E+2	1,7	-0.80	2.08	9.4E-3	high	2	1234		12
171	16:52:23.2	-43:18:03	G342.114+0.504	2.5	-25.1	2.6E+22	3.0E+4	3.5E+2	1,7	-0.48	0.86	2.7E-3	high	1			12
172	16:52:27.0	-44:31:03	G341.181-0.277	2.76	-43.7	3.1E+22	6.7E+4	2.3E+2	1,7	-1.17	1.92	5.9E-3	high	2			12
173	16:52:30.4	-44:28:36	G341.219-0.259	2.77	-44.5	6.5E+22	1.5E+4	1.0E+3	1	-0.58	1.42	7.2E-3	high	2	1		12
174	16:52:37.1	-44:28:17	G341.236-0.271	2.77	-44.2	8.5E+22	8.6E+3	1.8E+3	1,7	-0.90	2.21	1.4E-2	high	2	12		12
175	16:52:51.6	-44:28:04	G341.266-0.302	2.75	-43.3	1.0E+23	9.2E+3	1.8E+3	1,7	-0.64	1.69	1.1E-2	high	3			12
176	16:54:00.5	-43:16:19	G342.323+0.294	5.7	-114.5	2.2E+22	2.9E+3	3.7E+3	1,7	-0.30	0.59	4.1E-3	high	3			12
177	16:54:39.2	-43:52:14	G341.932-0.174	2.76	-42.8	1.0E+23	1.5E+4	3.9E+3	1	-0.28	0.86	1.0E-2	high	3			12
178	16:54:39.2	-43:51:28	G341.942-0.166	2.75	-42.0	1.9E+23	1.7E+4	4.7E+3	1	-0.36	1.21	1.7E-2	high	3			12
179	16:54:56.8	-45:09:07	G340.969-1.021	2.5	-24.1	2.8E+23	5.8E+4	1.3E+3	1	-0.32	1.03	9.5E-3	high	2	12		
180	16:58:17.2	-42:52:02	G343.128-0.062	2.58	-30.8	3.2E+23	2.0E+4	2.1E+3	1,7	-0.43	1.30	1.2E-2	high	3	134		12
181	16:59:30.8	-42:35:07	G343.489-0.064	2.55	-28.3	3.6E+22	2.4E+3	5.5E+2	1	-0.60	0.92	1.7E-3	high	3			12
182	17:00:33.2	-42:25:08	G343.738-0.112	2.55	-27.5	6.3E+22	1.3E+4	4.4E+2	1,7	-0.66	1.39	3.8E-3	high	2	3		12
183	17:00:50.1	-42:26:12	G343.756-00.164	2.55	-26.9	1.3E+3	1.3E+3		1,7	-0.82	0.70	2.0E-3	high				28
184	17:01:01.3	-42:48:08	G343.489-0.416	2.58	-28.7	4.0E+22	1.5E+4	6.6E+2	1	-0.43	0.57	2.1E-3	high	1			12
185	17:02:09.1	-41:46:49	G344.424+0.046	4.02	-66.3	1.0E+23	3.1E+3	6.3E+3	1,7	-0.70	1.54	1.5E-2	high	3	234		12
186	17:03:17.1	-42:25:58	G344.036-0.519	2.68	-24.0	3.4E+22	6.7E+3	8.5E+2	1	-0.29	0.82	2.8E-3	high	2			12

Table A.1: An Excerpt of the Physical Properties of Infall Sources.

No.	R.A. (J2000)	Dec. (J2000)	Alias	Dist. (kpc)	V_{LSR} (km s $^{-1}$)	$N(\text{H}_2)$ (cm $^{-2}$)	$n(\text{H}_2)$ (cm $^{-3}$)	Mass (M $_{\odot}$)	Lines	δv	V_{in} (km s $^{-1}$)	\dot{M}_{in} (M $_{\odot}$ yr $^{-1}$)	Type	Stage	Maser	Outflow	Ref.
(1)	(2)	(3)	(4)	(5)	(6)	(7)	(8)	(9)	(10)	(11)	(12)	(13)	(14)	(15)	(16)	(17)	(18)
187	17:03:26.2	-42:29:41	G344.004-0.579	2.52	-22.8	4.2E+22	3.3E+4	1.1E+3	1,7	-0.64	2.25	1.5E-2	high	2			12
188	17:03:30.0	-42:37:56	G343.902-0.672	2.58	-29.5	3.3E+22	1.4E+3	1.7E+4	1,7	-0.29	0.70	1.0E-2	high	2			12
189	17:04:07.1	-42:28:03	G344.102-0.662	2.67	-25.6	7.8E+22	6.7E+3	1.3E+3	1,7	-0.73	2.18	9.9E-3	high	3			12
190	17:05:23.3	-41:32:50	G344.977-0.292	2.71	-28.0	2.8E+22	7.7E+4	3.8E+2	1,7	-0.90	1.68	7.5E-3	high	1			12
191	17:07:53.9	-40:31:39	G346.076-0.056	5.23	-84.1	5.1E+22	2.0E+3	6.5E+3	1	-0.48	1.38	1.2E-2	high	3			12
192	17:08:01.5	-41:38:39	G345.196-0.744	1.33	-22.3	2.1E+22	3.4E+3	6.2E+3	1,7	-0.61	0.60	6.1E-3	high	3			12
193	17:11:19.1	-40:38:38	G346.369-0.647	1.31	5.8	3.0E+22	6.3E+3	9.3E+3	1,7	-1.42	0.49	8.1E-3	high	2			12
194	17:12:31.3	-38:19:09	G348.383+0.537	1.3	-7.2	3.9E+22	1.5E+5	2.5E+2	1	-0.48	0.61	2.6E-3	high	1			12
195	17:12:33.2	-38:19:57	G348.376+0.524	1.3	-7.3	5.8E+22	5.3E+4	2.0E+2	1	-0.41	0.73	1.9E-3	high	2			12
196	17:14:24.7	-38:32:34	G348.419+0.106	5.06	-104.9	2.0E+22	1.7E+4	1.2E+3	1,7	-0.45	0.91	5.3E-3	high	2			12
197	17:17:49.1	-36:09:14	G350.757+0.942	1.32	-9.1	6.9E+22	2.9E+3	4.7E+4	1,7	-0.42	0.97	3.6E-2	high	2			12
198	17:17:58.6	-36:13:23	G350.719+0.876	1.32	-6.5	2.2E+22	2.7E+3	9.8E+3	1	-0.42	0.56	6.6E-4	high	2			12
199	17:18:27.1	-36:13:33	G350.772+0.796	1.31	-4.7	2.3E+22	2.4E+5	2.3E+1	1	-0.63	0.52	5.2E-4	high	1			12
200	17:18:28.0	-36:12:47	G350.784+0.801	1.31	-4.4	1.9E+22	6.1E+4	5.8E+1	1	-0.89	0.33	3.9E-4	high	1			12
201	17:19:05.1	-36:06:42	G350.939+0.757	1.31	-4.2	4.5E+22	1.5E+5	7.1E+1	1,7	-0.64	1.32	2.4E-3	high	2			12
202	17:19:08.2	-36:06:59	G350.941+0.746	1.31	-3.8	6.0E+22	3.8E+4	1.9E+2	1,7	-0.78	1.51	3.3E-3	high	2			12
203	17:19:10.5	-39:00:22	G348.579-0.919	2.8	-14.7	9.3E+22	1.5E+4	1.1E+3	1,7	-0.46	1.13	5.9E-3	high	2	1234		12
204	17:19:11.6	-39:02:21	G348.554-0.941	1.31	-14.3	2.9E+22	1.1E+4	3.5E+2	1	-0.41	1.10	2.4E-3	high	2			12
205	17:19:12.2	-38:59:08	G348.599-0.912	2.8	-14.5	6.9E+22	2.0E+5	1.0E+4	1	-0.39	0.89	4.9E-2	high	2	3		12
206	17:19:18.2	-39:04:48	G348.533-0.982	1.31	-14.6	1.1E+23	2.7E+4	1.4E+4	1	-0.31	0.85	3.0E-2	high	3	234		12
207	17:19:20.3	-39:03:54	G348.549-0.979	2.78	-16.1	1.7E+23	1.2E+4	6.3E+2	1	-0.31	0.87	2.9E-3	high	3	1234		12
208	17:19:26.8	-37:11:01	IRAS17160-3707	4.97	-70.0	1.1E+4	1.3E+4	6	-0.47	1.66	3.8E-2	high	3	234	Y	12	
209	17:20:15.4	-35:59:29	G351.173+0.632	1.32	-5.0	6.5E+22	4.6E+3	4.8E+2	1	-0.33	0.78	1.6E-3	high	2			12
210	17:20:48.8	-35:45:07	G351.434+0.676	1.31	-3.3	1.9E+23	1.5E+5	4.4E+2	1	-0.26	0.73	4.4E-3	high	2			12
211	17:20:54.6	-35:45:13	G351.444+0.659	1.32	-4.2	8.3E+23	1.1E+5	3.4E+3	1	-0.31	1.08	2.3E-2	high	2	123		12
212	17:20:56.1	-37:00:52	G350.411-0.064	2.76	-27.0	5.4E+22	3.7E+3	1.4E+4	1,7	-0.39	0.90	1.6E-2	high	2	13		12
213	17:21:59.6	-35:27:43	G351.809+0.644	1.31	-2.2	4.0E+22	9.5E+4	7.2E+1	1	-0.61	0.78	1.2E-3	high	2			12
214	17:22:25.4	-37:05:10	G350.521-0.349	2.77	-22.7	5.1E+22	5.0E+3	1.1E+3	1	-0.40	0.86	3.2E-3	high	2	23		12
215	17:23:16.3	-34:48:47	G352.492+0.796	1.32	-2.9	1.2E+23	3.2E+4	1.4E+2	1	-0.33	0.74	1.3E-3	high	3			12
216	17:23:20.9	-34:48:42	G352.502+0.784	1.32	-1.6	5.2E+22	1.9E+5	3.8E+1	1	-1.01	1.89	2.5E-3	high	2			12
217	17:23:24.3	-34:48:31	G352.511+0.776	1.31	-1.2	3.5E+22	2.3E+4	2.6E+1	1,7	-0.74	1.27	6.3E-4	high	1			12

Table A.1: An Excerpt of the Physical Properties of Infall Sources.

No.	R.A. (J2000)	Dec. (J2000)	Alias	Dist. (kpc)	V_{LSR} (km s $^{-1}$)	$N(\text{H}_2)$ (cm $^{-2}$)	$n(\text{H}_2)$ (cm $^{-3}$)	Mass (M $_{\odot}$)	Lines	δv	V_{in} (km s $^{-1}$)	\dot{M}_{in} (M $_{\odot}$ yr $^{-1}$)	Type	Stage	Maser	Outflow	Ref.
(1)	(2)	(3)	(4)	(5)	(6)	(7)	(8)	(9)	(10)	(11)	(12)	(13)	(14)	(15)	(16)	(17)	(18)
218	17:23:50.3	-36:38:58	IRAS17204-3636	2.7	-17.7	1.5E+4	7.9E+2	6	-0.83	1.21	4.9E-3	high	3			1	
219	17:23:50.4	-36:38:59	G351.041-0.336	2.71	-18.5	1.1E+23	1.7E+4	7.6E+2	1,7	-0.37	1.05	4.5E-3	high	3			12
220	17:24:50.8	-34:10:21	G353.204+0.889	1.32	-2.6	4.2E+22	6.0E+2	2.3E+4	1	-0.34	0.32	2.6E-4	high	3			12
221	17:25:25.0	-36:12:45	IRAS17220-3609	5.96	-94.9	5.9E+3	2.0E+4	6	-0.77	4.71	1.2E-1	high	3	1234		1	
222	17:25:39.4	-34:31:04	G353.012+0.557	1.32	-0.7	3.3E+22	4.9E+4	1.0E+1	1,7	-0.67	1.70	5.8E-4	high	2			12
223	17:25:54.3	-34:32:25	G353.022+0.502	1.32	-3.6	3.5E+22	4.9E+3	3.0E+2	1	-0.40	1.11	1.7E-3	high				12
224	17:26:03.4	-34:16:19	G353.262+0.626	1.32	-4.2	2.5E+22	1.5E+5	2.2E+1	1,7	-0.64	0.72	6.0E-4	high				12
225	17:26:04.5	-35:30:00	G352.246-0.064	4.87	-90.6	1.4E+22	2.1E+3	4.5E+3	1,7	-0.27	0.66	4.6E-3	high	3			12
226	17:26:13.5	-34:31:54	G353.066+0.452.2	1.32	1.9	2.0E+3	2.0E+2	1,7	-0.63	1.20	1.1E-3	high	2			28	
227	17:26:19.2	-34:31:01	G353.089+0.444	1.32	-1.8	4.5E+22	2.3E+4	6.0E+1	1,7	-0.52	1.02	9.0E-4	high	3			12
228	17:26:24.9	-35:34:15	G352.226-0.161	4.85	-90.2	1.4E+22	7.8E+2	1,7	-0.63	1.75		high	3			12	
229	17:26:26.9	-35:33:39	G352.238-0.161	4.86	-91.8	3.2E+22	1.8E+3	1.6E+3	1	-0.39	0.98	3.2E-3	high	2			12
230	17:26:46.8	-33:59:26	G353.579+0.659	1.31	-1.1	4.5E+22	4.9E+4	2.3E+1	1,7	-0.64	1.09	6.5E-4	high	2			12
231	17:29:13.6	-34:32:53	G353.396-0.071	4.82	-49.6	9.8E+22	5.9E+3	4.3E+3	1	-0.31	1.21	1.2E-2	high	3			12
232	17:30:17.3	-33:13:51	G354.616+0.472	3.73	-20.3	1.9E+23	1.6E+4	2.6E+3	1,7	-0.29	0.78	7.4E-3	high	3	1234		12
233	17:30:33.8	-33:50:24	G354.139+0.089	4.82	-87.7	2.1E+22	8.0E+3	1.9E+3	1	-0.59	0.66	4.1E-3	high	2			12
234	17:33:50.5	-32:46:01	G355.412+0.102	1.32	4.8	6.2E+22	4.7E+3	1.8E+4	1	-0.35	0.81	1.9E-2	high	2			12
235	17:34:40.5	-33:48:42	G354.629-0.611	1.32	-2.9	2.4E+22	2.8E+4	1.2E+2	1,7	-0.38	0.78	1.2E-3	high	2			12
236	17:34:56.7	-33:05:33	G355.264-0.269	1.32	-2.9	8.5E+22	4.4E+4	1.7E+2	1,7	-0.50	1.48	3.2E-3	high	2			12
237	17:35:03.6	-32:39:48	G355.638-0.057	3.73	-19.8	2.3E+22			1,7	-0.68	2.18		high	2			12
238	17:35:11.7	-33:30:24	G354.944-0.537	1.32	-5.9	5.1E+22	2.2E+4	2.6E+2	1,7	-0.52	1.06	2.4E-3	high	1			12
239	17:35:38.5	-33:16:01	G355.196-0.486	1.32	-5.3	3.0E+22	5.6E+4	3.8E+2	1,7	-1.08	0.57	2.3E-3	high	2			12
240	17:36:14.1	-31:49:12	G356.482+0.189	1.33	-5.5	5.1E+22			1,7	-0.46	0.84		high	2			12
241	17:36:36.4	-24:11:31	G002.97+4.22	5.21	19.7	1.6E+21			9	-1.75			high	2		3	
242	17:42:15.3	-31:17:45	G357.609-0.617	1.32	2.6	4.4E+22			1	-0.29	0.55		high	2			12
243	17:42:50.3	-29:45:44	G358.979+0.084	5.93	-2.3	4.8E+22			1,7	-0.63	1.03		high	2			12
244	17:43:23.0	-30:18:48	G358.572-0.306	2.73	-4.3	3.2E+22			1,7	-0.64	1.15		high	1			12
245	17:43:24.1	-30:17:58	G358.586-0.302	2.73	-4.5	3.0E+22			1	-0.43	1.18		high	1			12
246	17:44:29.6	-29:42:18	G359.216-0.192	5.33	15.6	1.7E+22			1,7	-0.58	0.50		high	1			12
247	17:44:32.9	-29:42:45	G359.216-0.206	5.34	15.8	1.9E+22			1,7	-1.05	0.78		high	1			12
248	17:44:41.2	-28:53:40	G359.929+0.196	2.74	-3.5	4.3E+22			1	-0.66	1.49		high	1			12

Table A.1: An Excerpt of the Physical Properties of Infall Sources.

No.	R.A. (J2000)	Dec. (J2000)	Alias	Dist. (kpc)	V_{LSR} (km s $^{-1}$)	$N(\text{H}_2)$ (cm $^{-2}$)	Mass (M $_{\odot}$)	Lines	δv	V_{in} (km s $^{-1}$)	\dot{M}_{in} (M $_{\odot}$ yr $^{-1}$)	Type	Stage	Maser	Outflow	Ref.	
(1)	(2)	(3)	(4)	(5)	(6)	(7)	(8)	(9)	(10)	(11)	(12)	(13)	(14)	(15)	(16)	(17)	(18)
249	17:47:45.4	-29:02:15	G000.156-0.452	2.85	17.0	4.4E+22		1,7	-0.45	0.94	high	1	23			12	
250	17:47:45.4	-29:01:33	G000.166-0.446	2.85	16.2	6.3E+22		1	-0.29	0.59	high	3	23			12	
251	17:49:24.0	-28:48:46	G000.534-0.644	2.84	16.1	4.5E+22		1	-0.69	1.19	high	2				12	
252	17:49:30.6	-28:53:07	G000.484-0.702	2.83	14.2	5.2E+22		1	-1.56	3.27	high	2	1			12	
253	17:50:20.7	-28:52:12	G000.591-0.851	2.83	17.3	1.9E+22	4.1E+1	1	-0.36	0.94	high	1				12	
254	17:50:46.1	-26:39:49	G002.534+0.199	2.82	9.7	5.5E+22		1,7	-0.50	1.04	high	2	23			12	
255	17:53:33.8	-25:19:42	G004.003+0.339	2.94	12.5	3.7E+22	8.2E+3	6.0E+2	1,7	-0.52	0.85	2.5E-3	high	3	3	12	
256	17:53:35.9	-25:20:19	G003.998+0.327	2.94	12.4	2.5E+22		1	-0.69	0.97	high	3	3			12	
257	17:54:53.9	-26:11:07	G003.416-0.354	4.71	-25.3	4.9E+22		1	-0.57	1.89	high	1				12	
258	17:55:46.7	-26:16:47	G003.434-0.572	2.91	2.5	3.2E+22		1	-1.28	1.31	high	1				12	
259	17:57:48.7	-24:19:15	G005.359+0.014	2.94	12.7	3.1E+22	2.3E+4	2.3E+2	1,7	-0.62	0.78	1.7E-3	high	2		12	
260	17:58:44.5	-24:08:43	G005.617-0.082	4.67	-26.3	9.1E+22	7.4E+3	2.5E+3	1,7	-0.58	1.71	1.2E-2	high	2	123	12	
261	17:58:47.7	-25:17:40	G004.627-0.666	2.93	9.9	2.8E+22	3.4E+3	7.9E+3	1,7	-0.86	1.58	1.9E-2	high	2	1	12	
262	18:00:16.0	-23:59:57	G005.917-0.311	2.94	10.1	1.2E+22	1.3E+4	5.6E+3	1,7	-0.51	0.77	1.1E-2	high	1		12	
263	18:00:43.7	-24:04:57	G005.897-0.444	2.94	9.7	7.2E+22	1.1E+4	8.3E+2	1,7	-1.24	2.11	8.3E-3	high	3	123	12	
264	18:00:51.5	-24:10:19	G005.834-0.514	2.94	16.3	5.0E+22	4.2E+3	1.8E+3	1,7	-0.47	0.86	4.1E-3	high	3		12	
265	18:01:17.6	-22:41:43	G007.166+0.131	6.41	80.9	4.0E+22	1.6E+4	2.7E+3	1	-0.39	1.17	1.1E-2	high	2	123	12	
266	18:02:02.9	-23:53:13	G006.216-0.609	3.56	18.6	8.1E+22	9.2E+3	1.7E+3	1,7	-0.57	1.27	7.6E-3	high	2	1	12	
267	18:02:18.8	-22:45:03	G007.234-0.101	3.57	19.1	4.7E+22	1.4E+4	1.7E+3	1,7	-0.44	0.92	6.4E-3	high	1		12	
268	18:05:22.3	-21:44:37	G008.459-0.222	2.87	37.8	4.0E+22	1.5E+4	6.6E+2	1	-0.70	1.72	6.5E-3	high	2	1	12	
269	18:05:30.1	-21:49:37	G008.401-0.289	2.87	37.1	6.6E+22	1.0E+4	1.9E+3	7	-0.21	0.51	3.5E-3	high	3	3	12	
270	18:05:33.1	-21:49:36	G008.407-0.299	2.87	37.0	4.5E+22	4.3E+2	4.3E+2	1	-0.31	0.79	high	2	3		12	
271	18:05:44.4	-21:50:48	G008.411-0.347	2.87	38.0	3.8E+22	5.8E+3	1.3E+3	1,7	-1.19	1.51	6.6E-3	high	3		12	
272	18:06:19.0	-21:37:32	G008.67-0.36	2.86	36.0	1.8E+5		1	-0.44	0.40	4.0E-4	high	3	1234	14,15,19		
273	18:06:19.2	-21:37:27	G008.671-0.356	2.86	34.8	3.0E+23	1.5E+4	5.2E+3	1,7	-0.38	1.42	2.1E-2	high	3	1234	12	
274	18:06:23.4	-21:37:05	G008.684-0.367	2.87	37.1	1.3E+23	2.5E+4	3.5E+3	1,7	-0.56	2.63	3.6E-2	high	2	234	12	
275	18:06:24.8	-21:40:10	G008.642-0.397	2.87	38.9	4.7E+22	7.6E+2		7	-0.10	0.19	high	2			12	
276	18:06:28.8	-21:34:13	G008.736-0.362	2.87	39.4	5.5E+22	8.1E+3	2.1E+3	1	-0.53	1.42	9.5E-3	high	3	3	12	
277	18:06:36.7	-21:37:19	G008.706-0.414	2.87	39.0	9.1E+22	1.1E+4	6.3E+3	1	-0.29	0.72	1.1E-2	high	2	3	12	
278	18:06:49.3	-20:59:13	G009.284-0.147	3.81	41.7	5.2E+22	1.6E+4	2.1E+3	1,7	-0.62	1.15	9.5E-3	high	2		12	
279	18:08:16.7	-22:05:20	G008.486-0.979	2.91	15.8	4.9E+22	3.8E+4	7.9E+2	1	-0.52	0.82	4.8E-3	high	2	3	12	

Table A.1: An Excerpt of the Physical Properties of Infall Sources.

No.	R.A. (J2000)	Dec. (J2000)	Alias	Dist. (kpc)	V_{LSR} (km s $^{-1}$)	$N(\text{H}_2)$ (cm $^{-2}$)	$n(\text{H}_2)$ (cm $^{-3}$)	Mass (M_{\odot})	Lines	δv	V_{in} (km s $^{-1}$)	\dot{M}_{in} (M_{\odot} yr $^{-1}$)	Type	Stage	Maser	Outflow	Ref.
(1)	(2)	(3)	(4)	(5)	(6)	(7)	(8)	(9)	(10)	(11)	(12)	(13)	(14)	(15)	(16)	(17)	(18)
280	18:08:19.6	-22:04:29	G008.504-0.982	1.25	15.3	4.0E+22	6.4E+4	5.9E+2	1	-0.35	0.48	2.7E-3	high	2	3	12	
281	18:08:38.2	-19:51:49	IRAS18056-1952	7.96	68.5	8.3E+3	2.5E+4		6	-0.59	3.08	1.0E-1	high	3	1234		1
282	18:08:38.4	-19:51:52	G10.47+0.03	7.42	67.0	7.2E+5			1	0.42	1.6E-2	high	3	1234			14,16
283	18:08:46.5	-20:05:50	G010.284-0.114	1.25	14.1	1.1E+23	7.8E+3	2.6E+4	1,7	-0.35	1.19	4.2E-2	high	2	123		12
284	18:08:49.2	-20:05:54	G010.288-0.124	1.25	13.9	8.5E+22	1.2E+5	5.8E+2	1,7	-0.30	0.81	5.5E-3	high	3	123		12
285	18:09:20.8	-20:02:03	G010.404-0.201	1.25	11.5	4.4E+22	4.5E+3	3.0E+4	1,7	-1.20	1.53	4.9E-2	high	3	3		12
286	18:09:21.1	-20:16:10	G010.199-0.316	1.25	11.2	3.0E+22	5.5E+2		1,7	-0.64	2.63	high	1	1			12
287	18:10:05.7	-19:26:46	G011.004-0.071	2.85	28.4	4.8E+22	5.4E+4	1.0E+3	1,7	-1.22	1.77	1.4E-2	high	2			12
288	18:10:28.0	-19:56:04	G10.6-0.4	4.84	-3.0				1	-0.22	0.05	6.0E-4	high	3	1234		14
289	18:10:46.9	-17:34:15	G012.72+0.69	1.24	17.3	1.6E+22			1	-0.35	0.04		high	2			3
290	18:10:50.6	-17:55:46	G012.418+0.506	1.24	18.3	1.4E+23	1.6E+4	8.1E+2	1,7	-0.71	1.64	7.2E-3	high	3	13		12
291	18:11:31.3	-19:30:41	G011.109-0.397	4.85	0.3	8.9E+22	3.5E+3	6.3E+3	1,7	-0.71	1.93	2.0E-2	high	3	3		12
292	18:11:32.0	-19:30:39	G11.11-0.4	4.85	1.0				1				high	3	3		14,18
293	18:11:51.1	-17:31:30	G12.89+0.49	1.25					2	-0.45			high				19
294	18:11:58.6	-19:36:04	G011.082-0.534	2.85	29.5	9.1E+22	3.2E+4	1.9E+3	1	-0.32	0.79	7.7E-3	high	2	1		12
295	18:12:11.2	-18:41:35	G011.902-0.141	3.83	37.9	8.9E+22	7.2E+3	2.4E+3	1,7	-0.53	1.74	1.2E-2	high	3	234		12
296	18:13:56.3	-17:28:36	G013.169+0.077	3.86	49.7	3.1E+22	3.8E+4	6.3E+2	1	-0.62	1.45	7.2E-3	high	2			12
297	18:14:01.3	-17:28:39	G013.178+0.059	3.86	49.4	9.1E+22	6.1E+3	2.4E+3	1	-0.43	1.36	8.9E-3	high	2	123		12
298	18:14:08.2	-17:57:04	G012.77-0.19	2.95	35.6	1.4E+23			1	-0.61			high	3	3		3
299	18:14:10.0	-17:27:22	G013.213+0.039	3.87	51.9	5.8E+22	3.0E+3	5.1E+3	1	-0.29	0.64	5.5E-3	high	3			12
300	18:14:12.6	-17:57:34	G012.776-0.211	2.95	35.5	3.5E+22	1.3E+4	7.4E+2	1	-0.39	0.66	2.5E-3	high	1			12
301	18:14:22.1	-17:52:02	G012.87-0.20	2.95	35.5	1.0E+23			1	-0.12	0.36			2			3
302	18:14:36.8	-17:29:25	G013.234-0.071	3.85	38.1	3.0E+22	7.7E+4	7.1E+2	1	-0.73	1.31	8.9E-3	high	2			12
303	18:14:39.6	-17:48:36	G012.96-0.23	2.94	35.2	1.2E+23			1	-0.62	2.02			2	3		3
304	18:14:41.2	-17:29:23	G013.243-0.086	2.95	36.8	1.4E+23	1.9E+4	2.2E+3	1	-0.33	0.89	8.0E-3	high	2	13		12
305	18:14:41.8	-17:54:23	G012.878-0.287	2.93	33.4	5.4E+22	7.3E+4	8.3E+1	1,7	-0.50	1.28	2.0E-3	high	3			12
306	18:14:42.3	-17:37:10	G013.131-0.152	3.85	45.1	5.5E+22	9.1E+3	1.3E+3	1,7	-0.64	1.01	4.9E-3	high	3			12
307	18:15:37.3	+03:48:19	LDN 492	0.24	7.7	3.9E+21	6.5E+4		2,11	-0.35	0.04	4.4E-6	low	1			6,24,31
308	18:15:37.7	-17:34:06	G013.281-0.321	3.85	41.0	3.5E+22	2.4E+5	4.7E+2	1,7	-1.16	2.13	1.6E-2	high	2			12
309	18:15:39.9	-17:34:37	G013.28-00.34-MM1	3.85	41.3	2.9E+22			1,4	-0.59	1.09	1.5E-3	high	1	13		12
310	18:15:40.0	-17:34:44	G013.276-0.334	3.85	41.3	5.2E+22	5.6E+3	2.8E+3	1,7	-1.00	1.32	9.2E-3	high	1			12

Table A.1: An Excerpt of the Physical Properties of Infall Sources.

No.	R.A. (J2000)	Dec. (J2000)	Alias	Dist. (kpc)	V_{LSR} (km s $^{-1}$)	$N(\text{H}_2)$ (cm $^{-2}$)	$n(\text{H}_2)$ (cm $^{-3}$)	Mass (M_{\odot})	Lines	δv	V_{in} (km s $^{-1}$)	\dot{M}_{in} (M_{\odot} yr $^{-1}$)	Type	Stage	Maser	Outflow	Ref.
(1)	(2)	(3)	(4)	(5)	(6)	(7)	(8)	(9)	(10)	(11)	(12)	(13)	(14)	(15)	(16)	(17)	(18)
311	18:15:41.0	-17:33:18	G013.299-0.326	3.85	40.5	2.5E+22	2.5E+4	5.2E+2	1,7	-0.83	1.45	5.6E-3	high	1			12
312	18:16:22.0	-16:53:02	G013.97-0.15	3.85	40.2	4.5E+22			1,9	-0.53	0.09			2			3
313	18:16:38.2	-16:51:09	G014.02-0.19	3.85	40.0	7.0E+22			1,9	-0.47	0.45			2			3
314	18:16:40.7	-16:45:48	G014.11-0.16	3.86	39.1	2.8E+22			1	-0.48	0.34			2			3
315	18:16:59.4	-18:02:30	LDN 328-IRS	1.25	6.7				9	-0.66	0.04	7.2E-7	low	2			26
316	18:17:01.3	-16:38:48	G014.25-0.17	3.86	38.3	7.1E+22			1	-0.78		high		2			3
317	18:17:02.3	-16:38:21	G014.26-0.17	3.86	38.5	6.4E+22			1,9	-0.85	0.44			2			3
318	18:17:16.5	-17:01:16	G013.97-00.45-MM1	3.06	20.0				1	-0.73	0.31			high			13
319	18:17:34.8	-17:06:52	G013.91-00.51-MM1	3.02	23.0	7.7E+22			1,3	-0.64	0.69	2.2E-3	high				13
320	18:17:35.1	-17:06:53	G013.902-0.516	3.01	23.3	4.8E+22	1.4E+4	7.8E+2	1,7	-1.59	1.00	4.0E-3	high	2			12
321	18:18:12.7	-16:49:34	G014.227-0.511	1.84	19.4	1.6E+23	1.2E+4	1.5E+3	1,7	-0.51	1.16	7.0E-3	high	2	123		12
322	18:18:13.1	-16:57:20	G014.114-00.574	3.06	20.1	1.3E+3	8.0E+2		1,7	-0.52	2.00	3.8E-3	high	2	13		28
323	18:18:57.2	-13:40:14	G017.09+0.82	1.87	22.4	3.9E+22			1,9	-0.85	0.04			2			3
324	18:19:02.9	-16:30:29	G014.63-00.57-MM3	1.83	17.4	5.2E+22			4			high					13
325	18:19:11.2	-16:29:56	G014.626-0.562	1.83	18.0	2.8E+22	1.9E+3	5.4E+2	1,7	-0.66	1.25	2.1E-3	high	1	123		12
326	18:19:12.1	-13:33:32	G017.19+00.81-MM3	1.87	22.7	5.3E+22			1,4	-0.35	1.65	2.8E-3	high	2			13
327	18:19:12.5	-16:19:49	G014.777-0.487	3.08	21.8	2.3E+22	4.9E+3	5.0E+3	1	-0.46	0.52	5.2E-3	high	2			12
328	18:19:12.9	-13:33:46	G017.19+00.81-MM2	1.88	22.8	1.7E+23			1	-0.48	0.66	3.1E-3	high	3			13
329	18:19:14.3	-16:30:41	G014.63-00.57-MM2	1.84	18.4	1.5E+23			3,4	-0.78		high		123			13
330	18:19:15.2	-16:29:59	G014.63-00.57-MM1	1.84	18.6	2.6E+23			3,4,5	-2.06	2.70	2.2E-2	high		123		13
331	18:19:17.4	-16:44:04	G014.39-00.75A-MM2	1.83	17.6				1,4	-0.45		high					13
332	18:19:19.0	-16:43:49	G014.39-00.75A-MM1	1.83	17.8	5.7E+22			1,4	-0.52		high					13
333	18:19:33.3	-16:45:01	G014.39-00.75B-MM3	4.88	5.7E+22				1	-5.79		high					13
334	18:20:24.8	-16:11:35	M17S	1.85	20.0	5.0E+5			1	1.40	4.0E-4	high	3	1234			14,15
335	18:20:50.8	-14:06:01	G016.93+00.24-MM1	1.5	23.8	4.2E+22			1	-0.62		high					13
336	18:21:09.1	-14:31:49	IRAS18182-1433	3.84	59.1	1.4E+4	1.3E+3		1,3,12	-0.44		high		2	1234	Y	27
337	18:21:09.2	-14:31:47	IRAS18182-1433	3.84	59.0	1.4E+4	1.3E+3		6	-0.35	1.99	1.1E-2	high	3	1234	Y	1
338	18:21:10.0	-14:31:44	IRAS18182-1433	3.84	59.0	6.0E+22			1	1.74	1.6E-2	high	2	1234	Y	14,17	
339	18:25:01.8	-13:09:06	G018.26-00.24-MM5	3.93	66.6				4			high					13
340	18:25:04.5	-13:08:27	G018.26-00.24-MM4	3.95	68.8	5.7E+22			5	-1.14		high		1234			13
341	18:25:05.6	-13:08:20	G018.26-00.24-MM3	3.94	68.6	7.1E+22			1,4,5	-1.12	6.10	1.6E-2	high		1234		13

Table A.1: An Excerpt of the Physical Properties of Infall Sources.

No.	R.A. (J2000)	Dec. (J2000)	Alias	Dist. (kpc)	V_{LSR} (km s $^{-1}$)	$N(\text{H}_2)$ (cm $^{-2}$)	$n(\text{H}_2)$ (cm $^{-3}$)	Mass (M $_{\odot}$)	Lines	δv	V_{in} (km s $^{-1}$)	\dot{M}_{in} (M $_{\odot}$ yr $^{-1}$)	Type	Stage	Maser	Outflow	Ref.
(1)	(2)	(3)	(4)	(5)	(6)	(7)	(8)	(9)	(10)	(11)	(12)	(13)	(14)	(15)	(16)	(17)	(18)
342	18:25:06.4	-13:08:51	G018.26-00.24-MM2	3.94	67.8	8.9E+22			1,4,5	-1.03			high	2	1234	13	
343	18:25:10.7	-12:42:28	IRAS18223-1243	3.24	45.5			1	-0.31			high	2			27	
344	18:25:11.8	-13:08:04	G018.26-00.24-MM1	3.94	68.4	9.8E+22			1,4,5	-1.18			high	2	13	13	
345	18:25:54.4	-11:52:34	G019.472+0.171	1.5	19.5	1.4E+23	1.3E+3	2.8E+4	1	-0.51	2.58	5.2E-2	high	2	1234	12	
346	18:27:38.3	-11:56:40	G19.61-0.23	3.27	43.0	3.4E+16	4.6E+6	1.5E+1	1,13,15	-0.37	0.21	1.4E-3	high	3	1234	10,14,16,20	
347	18:28:10.7	-11:28:48	G20.08-0.14	4.06	42.0			1	0.05	3.0E-4	high	3	1234		14,15,16		
†348	18:29:47.5	+01:17:01	Serp S68N	0.24	8.8				12	-1.61			low	2	14	Y	22
†349	18:29:51.2	+01:16:41	Serp SMM 5	0.24	8.4				11,12	-0.74			low	2	14	Y	22
†350	18:29:56.7	+01:13:16	Serp SMM 4	0.24	8.1				2,3,11,12	-0.40			low	2	13	Y	22
351	18:30:00.2	+01:02:12	G031.41+5.24	0.24	8.3	9.7E+21			1	-1.22							3
352	18:30:02.3	-12:15:38	IRAS18272-1217	3.29	34.0				1	-1.20			high	2			27
†353	18:30:14.4	-01:33:33	J1830144-013333	0.24	8.1				9	-0.24	0.17	8.1E-6	low	2			26
†354	18:30:15.6	-02:07:19	J1830156-020719	0.24	6.7				9	-0.90	0.27	5.5E-5	low	2			26
†355	18:30:16.2	-01:52:52	J1830162-015252	0.24	6.7				9	-0.83	0.22	2.0E-5	low	2			26
356	18:31:35.4	-01:54:21	G028.97+3.54	0.24	7.2	1.4E+22			1,9	-1.29	0.44			2			3
357	18:31:43.3	-09:22:28	IRAS18290-0924	4.74	84.3				2,3	-0.34			high	2	1234		27
358	18:32:14.5	-01:59:24	G028.97+3.36	0.24	7.3	2.5E+22			1,9	-1.25				2			3
†359	18:32:17.2	-01:59:11	G028.97+3.35	0.24	7.3	2.3E+22			1	-2.80				2			3
†360	18:32:42.4	-02:47:56	J1832424-024756	0.24	6.3				9	-0.47	0.10	4.3E-6	low	2			26
361	18:33:15.2	-00:46:22	G030.17+3.69	0.24	9.1	6.4E+21			1,9	-0.46							3
362	18:34:23.5	-08:32:20	G023.28-00.12-MM1	5.3	99.0	6.5E+22			1	-0.47			high	3			13
363	18:36:18.3	-07:41:00	G024.37-00.15-MM2	3.65	56.2	4.4E+22			1,5	-1.11			high				13
364	18:36:27.8	-07:40:24	G024.37-00.15-MM1	3.6	59.2	4.9E+22			1,4	-0.59			high	1			13
365	18:36:27.9	-07:40:25	IRAS18337-0743	3.64	57.9				1	-0.52			high	2	1		27
366	18:37:12.2	-07:11:23	G024.94-00.15-MM2	3.79	48.2	5.5E+22			1,4	-0.66	3.00	6.2E-3	high	3			13
367	18:37:19.7	-07:11:41	G024.94-00.15-MM1	3.79	47.4	6.5E+22			1,3,4,5	-0.80	1.34	3.3E-3	high	3			13
368	18:37:21.3	-07:33:07	G024.61-00.33-MM2	3.77	43.6	3.5E+22			4	-0.07			high				13
369	18:37:23.1	-07:31:39	G024.61-00.33-MM1	3.77	42.8	5.9E+22			1,4,5	-0.72			high				13
†370*	18:38:08.1	-06:46:52	G025.382-00.147	5.77	96.7	2.0E+6	4.7E+1		10	1.30	2.0E-3	high	2	134	11		
†371*	18:38:40.3	-05:35:06	IRAS18360-0537	6.06	103.5	8.0E+6	1.0E+1		13	1.50	1.5E-3	high	2	134	8		
372	18:39:04.7	-06:24:21	G025.82-0.18	5.47	93.7	5.6E+22			1	-0.37	1.53	high	2	1234	3		

Table A.1: An Excerpt of the Physical Properties of Infall Sources.

No.	R.A. (J2000)	Dec. (J2000)	Alias	Dist. (kpc)	V_{LSR} (km s $^{-1}$)	$N(\text{H}_2)$ (cm $^{-2}$)	Mass (M_{\odot})	Lines	δv	V_{in} (km s $^{-1}$)	\dot{M}_{in} (M_{\odot} yr $^{-1}$)	Type	Stage	Maser	Outflow	Ref.	
(1)	(2)	(3)	(4)	(5)	(6)	(7)	(8)	(9)	(10)	(11)	(12)	(13)	(14)	(15)	(16)	(17)	(18)
373	18:39:36.8	-05:54:42	G026.32-0.07	5.87	100.3	2.7E+22		1,9	-0.50	1.21		2					3
374	18:39:55.9	-05:38:52	IRAS18372-0541	1.75	23.6		1	-0.59			high	2	23				27
375	18:43:01.8	-04:14:27	G028.20-0.07	5.68	97.1	5.1E+22		1	-0.26	0.06	high	2	13	Y			3
376	18:45:12.2	-02:01:12	IRAS18426-0204	1.78	15.0			12	-0.41		high	2	23				27
377	18:46:22.4	-02:14:20	IRAS18437-0216	7.15	110.8		1,3,12	-0.40		high	2	3					27
378	18:47:33.0	-01:12:36	G31.41+0.31	5.17	97.0		1	-0.65		high	3	1234					14,15
379	18:47:34.4	-01:12:46	G31.41+0.31	14.33			2	-0.65		high	3	1234					19
380	18:47:36.8	-03:15:15	G029.60-0.63	4.27	77.2	3.6E+22		1	-0.98	1.77	8.9E-3	high	2	23			3
381	18:47:41.9	-01:52:13	G030.90+00B-MM2	5.42	92.8		1,4	-0.42	1.76	9.4E-3	high						13
382	18:47:48.2	-01:51:30	G030.90+00C-MM3	5.47	94.3	4.3E+22		1,4	-0.27		high						13
383	18:48:39.7	-03:03:56	IRAS18460-0307	4.38	83.7			1,12	-0.64		high	2					27
384	18:49:52.2	-00:18:57	IRAS18472-0022	2.51	49.0			1,12	-0.57		high	2					27
385	18:52:20.3	+00:26:20	G033.42+0.00	2.02	10.6	4.0E+21		1	-1.02			2	23				3
386	18:53:16.7	+01:14:43	G034.25+0.16	5.17	58.1	1.9E+23		1,9	-3.55			2	1234				3
388	18:53:18.4	+01:15:00	IRAS18507+0110	3.33	58.5	7.6E+4	1.6E+3	6	-0.66	4.83	5.3E-2	high	3	1234			1
387	18:53:18.4	+01:14:57	W44	3.33	57.8		1,2,10	-0.27			high	3	1234				19,20
389	18:53:18.5	+01:14:58	G34.26+0.15	5.17	58.0	3.6E+5		1	1.50	1.4E-3	high	3	1234	Y			14,15
†390	18:53:18.6	+01:14:58	G34.26+0.15	13.99		1.1E+8	76(11)	1,10,13	1.00	1.0E-4	high	3	1234	Y			5
391	18:53:23.2	+01:53:16	G034.85+00.43-MM1	3.21	55.7		4			high							13
392	18:54:40.6	+01:38:04	IRAS18521+0134	5.07	76.0			1,2,12	-0.89		high	2	12				27
393	18:56:58.2	+01:18:44	G034.71-00.63-MM2	2.51	45.8	5.2E+22		1,3	-0.35		high						13
394	18:57:05.2	+02:06:29	G035.49-00.30A-MM1	3.99	55.6	6.6E+22		1,4	-0.66	7.40	1.7E-2	high	3				13
395	18:57:08.1	+02:10:47	G035.49-00.30B-MM3	2.5	45.9	4.2E+22		4	-0.18		high						13
396	18:57:08.4	+02:09:01	G035.49-00.30B-MM2	2.5	45.4	5.3E+22		4	-0.20	0.84	1.4E-3	high					13
397	18:57:40.7	+01:16:09	G034.77-00.81-MM1	2.48	43.7			1,4	-0.76		high						13
398	18:57:53.3	+04:18:17	IRAS18553+0414	0.92	10.0			1,2,12	-0.57		high	2	134				27
399	18:59:04.7	+03:38:57	G037.05-0.03	4.58	81.3	3.3E+22		1	-0.29			2	234				3
400	19:01:54.0	+04:12:49	G037.87-00.40	4.2	58.8			1			high	3	34				14,18
401	19:01:55.3	+02:07:55	G036.02-1.36	2.18	31.8	8.6E+21		1,9	-0.60	0.26							3
402	19:03:44.7	+05:33:45	G039.28-0.19	4.06	70.5	2.2E+22		9	-0.34			2					3
403	19:03:45.1	+05:40:45	IRAS19012+0536	3.7	65.8			2,3,12	-0.65		high	2	1234	Y			27

Table A.1: An Excerpt of the Physical Properties of Infall Sources.

No.	R.A. (J2000)	Dec. (J2000)	Alias	Dist. (kpc)	V_{LSR} (km s $^{-1}$)	$N(\text{H}_2)$ (cm $^{-2}$)	Mass (M $_{\odot}$)	Lines	δv	V_{in} (km s $^{-1}$)	\dot{M}_{in} (M $_{\odot}$ yr $^{-1}$)	Type	Stage	Maser	Outflow	Ref.	
(1)	(2)	(3)	(4)	(5)	(6)	(7)	(8)	(9)	(10)	(11)	(12)	(13)	(14)	(15)	(16)	(17)	(18)
404	19:07:32.0	+05:15:46	G039.45-1.17	0.36	12.7	3.8E+21		1	-0.36	0.06			2				3
405	19:10:34.0	+09:08:24	G043.24-00.05	0.29	7.3			1	1.27	5.6E-2	high	3	13				14,18
406	19:19:48.4	+14:02:27	IRAS19175+1357	0.79	14.6			3	-0.32		high	2	3				27
407	19:22:42.6	+14:09:44	G049.07-0.33	5.13	60.4	3.0E+22		1	-0.54		high	2	13				3
408	19:24:19.7	+14:38:03	IRAS19220+1432	5.35	68.8			1,2,3,12	-0.40		high	2	2				27
409	19:26:52.8	+13:49:35	G049.25-1.38	0.06	5.7	5.9E+21		9	-1.64								3
410	19:29:04.2	+17:55:16	G053.10+0.11	1.31	22.2	8.9E+21		1	-0.21	0.09			2				3
411	19:29:08.9	+17:55:14	G053.11+0.09	1.31	22.0	1.1E+22		1	-0.30	0.19			2				3
412	19:29:12.7	+17:55:52	G053.12+0.08	1.31	22.3	2.4E+22		1,9	-0.58	0.12			2				3
413	19:29:12.9	+17:56:59	G053.14+0.09	1.32	22.3	1.5E+22		1,9	-0.83	0.03			2				3
414	19:30:19.6	+17:44:19	G053.08-0.24	1.43	23.6	6.5E+21		1	-0.99				2				3
415	19:30:55.7	+18:29:55	G053.81-00.00-MM1	1.56	24.1	6.9E+22		1,4	-0.34	7.40	9.6E-3	high					13
†416	19:37:01.4	+07:34:07	B335 SMM1	0.3	8.4			2,11,12	-0.46				2			Y	22
†417	19:41:04.5	+10:57:02	LDN 694-2	0.4	9.6	4.6E+21	1.8E+4	2,11	-0.46	0.05	4.9E-6	low	1				6,24,31
418	19:43:11.0	+23:44:06	IRAS19410+2336	2.16	22.4			1,3,12	-0.64				2				27
419	19:43:29.0	+23:40:22	IRAS19413+2332	2.16	20.8			1,3,12	-0.48				3				27
420	19:46:20.0	+24:35:29	G060.88-00.13	2.17	23.3			1	-0.93				3				14,18
†421	20:10:13.1	+27:28:17	IRAS20081+2720	0.09	5.7			1	-0.93				2				27
422	20:19:39.0	+40:56:38	G78.438+2.659	2.17	3.3			1	-0.93				3				14,18
423	20:27:25.7	+37:22:52	SH 2-106 FIR	3.41	-1.0			1	-0.34				34				20
†424	20:31:15.2	+40:22:21	G079.24+0.53	2.59	0.3	2.6E+22		1	-0.40	0.71			2				3
425	20:34:19.9	+40:31:12	G079.71+0.15	2.53	1.0	4.9E+21		1,9	-0.57	0.12			2				3
426	20:34:58.8	+41:34:47	IRAS20332+4124	2.65	-2.0			1,12	-0.41				2				27
427	20:35:51.9	+43:02:36	G081.90+1.43	2	11.0	4.8E+21		1,9	-1.77	0.02							3
428	20:35:56.7	+42:48:48	G081.72+1.28	2.19	3.7	1.1E+22		1,9	-0.72	0.16							3
429	20:39:00.7	+42:23:07	G081.72+0.57	2.29	-3.1	1.4E+23		1	-0.69	0.97	3.4E-2						3
430	20:39:00.9	+42:22:50	W75OH	2.29	-3.3			1,2,10,11	-0.39				2				19,20
431	20:39:01.0	+42:19:53	G081.68+0.54	1.55	-8.2			1	0.26	3.6E-4	high	3	123				14,18
432	20:39:06.5	+68:02:13	LDN 1157	0.87	2.7			2,11,12	-0.33		low	2	13				22
433	20:40:56.6	+67:23:04	LDN 1148B	0.87	2.6			9	-1.14	0.11	2.3E-6	low	2				26
434	20:42:39.2	+42:25:23	G082.17+0.07	1.67	10.1	1.0E+22		1,9	-0.29	0.01			2				3

Table A.1: An Excerpt of the Physical Properties of Infall Sources.

No.	R.A. (J2000)	Dec. (J2000)	Alias	Dist. (kpc)	V_{LSR} (km s $^{-1}$)	$N(\text{H}_2)$ (cm $^{-2}$)	Mass (M_{\odot})	Lines	δv	V_{in} (km s $^{-1}$)	\dot{M}_{in} (M_{\odot} yr $^{-1}$)	Type	Stage	Maser	Outflow	Ref.	
(1)	(2)	(3)	(4)	(5)	(6)	(7)	(8)	(9)	(10)	(11)	(12)	(13)	(14)	(15)	(16)	(17)	(18)
†435	20:42:58.8	+67:48:18	LDN 1155C-2	0.87	1.6	1.9E+21	6.6E+3	11	-0.47	0.07	3.9E-6	low	1				6,24
†436	20:43:30.0	+67:52:42	LDN 1155C-1	0.87	2.9	2.1E+21	5.1E+4	11	-0.48	0.09	2.3E-5	low	1				6,24
437	20:49:27.8	+41:25:54	G082.18-1.54	1.56	2.8	8.4E+21		9	-0.12								3
438	20:49:30.8	+41:27:23	G082.21-1.53	1.56	2.7	1.0E+22		9	-0.21		2.0E-4		2				3
439	20:58:15.6	+43:48:54	G085.05-1.25	5.12	-37.5	1.1E+22		1,9	-0.82	0.41		2		Y			3
†440	21:00:13.2	+50:20:50	LDN 981-1	1.61	0.0	1.2E+21	5.0E+3	11	-0.39	0.10	1.1E-5	low	1				6,24
441	21:02:21.2	+67:54:20	IRAS 21017+6742	0.87	2.9			9	-0.62	0.22	1.7E-5	low	2		Y		26
442	21:02:27.3	+67:54:18	J21022744+6754186	0.87	2.8			9	-0.63	0.16	1.0E-5	low	2		Y		26
443	21:44:57.0	+47:41:52	J21445706+4741529	0.67	1.6			9	-0.58	0.16	1.2E-5	low	2		Y		26
444	22:15:09.0	+58:49:09	IRAS22134+5834	2.81	18.5			1			high		2	3	Y		14,17
†445	22:28:33.3	+62:58:29	G107.50+4.47	0.78	-2.1	2.5E+22		1,9	-0.47		1.0E-4		2		Y		3
446	22:29:59.4	+75:14:03	IRAS 22290+7458	0.77	-4.0			9	-0.84	0.24	1.1E-5	low	2				26
†447	22:37:02.3	+58:57:21	LDN 1197	0.77	-3.1	2.0E+21	2.7E+4	11	-0.41	0.05	2.2E-6	low	1				6,24
448	22:38:47.1	+75:11:29	LDN 1251B	0.77	1.0			11,12	-0.73		low		2	3	Y		22
449	22:47:13.0	+62:11:41	G108.99+2.73	0.8	-10.5	2.6E+22		1,9	-0.44	0.16		2					3
†450	22:56:17.9	+62:01:49	Cep A	0.79	-10.0	1.0E+6		1,10	-0.59	0.23	1.7E-5	high	3	1234	Y		14,15,20
451	22:58:15.9	+62:35:29	G110.32+2.52	0.79	-12.1	1.4E+22		1,9	-0.73	0.08							3
452	23:01:58.6	+61:30:44	G110.40+1.67	0.79	-11.2	5.8E+21		1	-1.56								3
†453	23:03:13.1	+61:42:26	IRAS23011+6126	0.79	-11.0			2	-0.41		low		2	13	Y		25
454	23:13:44.9	+61:26:51	NGC7538	2.69	-56.0			1,11	-0.34		high		3	1234	Y		20,21
455	23:17:21.0	+59:28:49	IRAS23151+5912	2.7	-56.0			1			high		2	13	Y		14,17
†456	23:25:46.5	+74:17:38	CB 244	0.7	3.8			2	-1.02		low		2	Y			25

References

- Beltrán, M. T., & de Wit, W. J. 2016, A&A Rev., 24, 6 1
- Beuther, H., Sridharan, T. K., & Saito, M. 2005, The Astrophysical Journal, 634, L185 2, 13
- Bonnell, I. A., & Bate, M. R. 2002, Monthly Notices of the Royal Astronomical Society, 336, 659 2
- Bonnell, I. A., Vine, S. G., & Bate, M. R. 2004, Monthly Notices of the Royal Astronomical Society, 349, 735 2
- Cesaroni, R., Galli, D., Lodato, G., Walmsley, C. M., & Zhang, Q. 2007, in Protostars and Planets V, ed. B. Reipurth, D. Jewitt, & K. Keil, 197 1
- Churchwell, E., Sievers, A., & Thum, C. 2010, A&A, 513, A9 2
- Contreras, Y., Sanhueza, P., Jackson, J. M., et al. 2018, The Astrophysical Journal, 861, 14 2, 5
- Cunningham, N., Lumsden, S. L., Moore, T. J., Maud, L. T., & Mendigutía, I. 2018, Monthly Notices of the Royal Astronomical Society, 477, 2455 2, 3
- De Vries, C. H., & Myers, P. C. 2005, The Astrophysical Journal, 620, 800 11
- Di Francesco, J., Myers, P. C., Wilner, D. J., Ohashi, N., & Mardones, D. 2001, The Astrophysical Journal, 562, 770 5
- Djordjevic, J. O., Thompson, M. A., Urquhart, J. S., & Forbrich, J. 2019, MNRAS, 487, 1057 8
- Evans, N. J. 1999, Annual Review of Astronomy and Astrophysics, 37, 311 2, 3, 9
- Faúndez, S., Bronfman, L., Garay, G., et al. 2004, Astronomy and Astrophysics, 426, 97 5
- Fuller, G. A., Williams, S. J., & Sridharan, T. K. 2005, Astronomy and Astrophysics, 442, 949 2, 3, 5, 10
- Gregersen, E. M. 1998, Collapse and Beyond: an Investigation of the Star Formation Process, PhD thesis, THE UNIVERSITY OF TEXAS AT AUSTIN 9
- Gregersen, E. M. 2000, The Astrophysical Journal, 533, 440 2, 5
- Gregersen, E. M., Evans II, N. J., Zhou, S., & Choi, M. 1997, The Astrophysical Journal, 484, 256 5
- Guzmán, A. E., Sanhueza, P., Contreras, Y., et al. 2015, Astrophysical Journal, 815, 130 3
- He, Y. X., Zhou, J. J., Esimbek, J., et al. 2015, Monthly Notices of the Royal Astronomical Society, 450, 1926 2, 4, 5, 11
- He, Y. X., Zhou, J. J., Esimbek, J., et al. 2016, Monthly Notices of the Royal Astronomical Society, 461, 2288 2, 3, 5, 8, 11
- Hogerheijde, M. R., & Van Der Tak, F. F. 2000, Astronomy and Astrophysics, 362, 697 11
- Keown, J., Schnee, S., Bourke, T. L., et al. 2016, The Astrophysical Journal, 833, 97 2, 3, 5, 11
- Keto, E., Caselli, P., & Rawlings, J. 2015, Monthly Notices of the Royal Astronomical Society, 446, 3731 2

- Kim, M.-R., Lee, C. W., Maheswar, G., Myers, P. C., & Kim, G. 2021, *The Astrophysical Journal*, 910, 112 [2](#), [5](#), [13](#)
- Klaassen, P. D., Testi, L., & Beuther, H. 2012, *Astronomy and Astrophysics*, 538, A140 [2](#), [5](#)
- Klaassen, P. D., & Wilson, C. D. 2007, *The Astrophysical Journal*, 663, 1092 [5](#)
- Klaassen, P. D., & Wilson, C. D. 2008, *The Astrophysical Journal*, 684, 1273 [2](#), [5](#)
- Klassen, M., Pudritz, R. E., Kuiper, R., Peters, T., & Banerjee, R. 2016, *The Astrophysical Journal*, 823, 28 [1](#)
- Kurtz, S., Churchwell, E., & Wood, D. O. S. 1994, *The Astrophysical Journal Supplement Series*, 91, 659 [5](#)
- Lee, C. W., & Myers, P. C. 2011, *The Astrophysical Journal*, 734, 60 [2](#), [5](#)
- Lee, C. W., Myers, P. C., & Tafalla, M. 1999, *The Astrophysical Journal*, 526, 788 [2](#), [9](#)
- Lee, C. W., Myers, P. C., & Tafalla, M. 2001, *The Astrophysical Journal Supplement Series*, 136, 703 [2](#), [5](#), [11](#)
- Leung, C. M., & Brown, R. L. 1977, *The Astrophysical Journal*, 214, L73 [9](#)
- Li, Y., Xu, Y., Sun, Y., et al. 2019, *The Astrophysical Journal Supplement Series*, 242, 19 [6](#), [14](#)
- Li, Z. Y., Banerjee, R., Pudritz, R. E., et al. 2014, in *Protostars and Planets VI*, ed. H. Beuther, R. S. Klessen, C. P. Dullemond, & T. Henning, 173 [14](#)
- Liu, S.-Y., Su, Y.-N., Zinchenko, I., et al. 2020, *The Astrophysical Journal*, 904, 181 [2](#), [5](#)
- Liu, T., Wu, Y., & Zhang, H. 2013, *The Astrophysical Journal*, 776, 29 [2](#), [5](#), [11](#), [13](#)
- Liu, T., Wu, Y., Zhang, Q., et al. 2011, *The Astrophysical Journal*, 728 [2](#), [5](#)
- Mardones, D., Myers, P. C., Tafalla, M., et al. 1997, *The Astrophysical Journal*, 489, 719 [2](#), [3](#), [5](#), [9](#), [10](#)
- Maud, L. T., Moore, T. J., Lumsden, S. L., et al. 2015, *Monthly Notices of the Royal Astronomical Society*, 453, 645 [6](#), [14](#)
- McKee, C. F., & Tan, J. C. 2002, *Nature*, 416, 59 [1](#)
- McKee, C. F., & Tan, J. C. 2003, *The Astrophysical Journal*, 585, 850 [1](#)
- Motte, F., Bontemps, S., & Louvet, F. 2018, *Annual Review of Astronomy and Astrophysics*, 56, 41 [2](#), [3](#)
- Myers, P. C., Mardones, D., Tafalla, M., Williams, J. P., & Wilner, D. J. 1996, *The Astrophysical Journal*, 465, L133 [11](#)
- Padoan, P., Haugbølle, T., & Nordlund, Å. 2014, *The Astrophysical Journal*, 797, 32 [2](#), [13](#)
- Peretto, N., Fuller, G. A., Duarte-Cabral, A., et al. 2013, *Astronomy and Astrophysics*, 555, A112 [2](#), [11](#)
- Qin, S. L., Schilke, P., Wu, J., et al. 2016, *Monthly Notices of the Royal Astronomical Society*, 456, 2681 [2](#), [5](#), [11](#), [13](#)

- Qiu, K., Zhang, Q., Beuther, H., & Fallscheer, C. 2012, *The Astrophysical Journal*, 756, 170 [2](#), [5](#), [13](#)
- Redman, M. P., Khanzadyan, T., Loughnane, R. M., & Carolan, P. B. 2008, in *Astronomical Society of the Pacific Conference Series*, Vol. 387, *Massive Star Formation: Observations Confront Theory*, ed. H. Beuther, H. Linz, & T. Henning, 38 [3](#)
- Reid, M. J., Dame, T. M., Menten, K. M., & Brunthaler, A. 2016, *The Astrophysical Journal*, 823, 77 [6](#)
- Reid, M. J., Menten, K. M., Brunthaler, A., et al. 2019, *The Astrophysical Journal*, 885, 131 [6](#), [7](#)
- Reiter, M., Shirley, Y. L., Wu, J., et al. 2011, *The Astrophysical Journal*, 740, 1 [2](#), [5](#)
- Rygl, K. L. J., Wyrowski, F., Schuller, F., & Menten, K. M. 2013, *Astronomy and Astrophysics*, 549, A5 [2](#), [3](#), [5](#), [8](#), [10](#), [12](#)
- Saral, G., Audard, M., & Wang, Y. 2018, *Astronomy and Astrophysics*, 620, A158 [2](#), [4](#), [5](#), [12](#)
- Sarrasin, E., Abdallah, D. B., Wernli, M., et al. 2010, *MNRAS*, 404, 518 [3](#)
- Schnee, S., Brunetti, N., Di Francesco, J., et al. 2013, *The Astrophysical Journal*, 777, 121 [2](#)
- Schöier, F. L., Van Der Tak, F. F., Van Dishoeck, E. F., & Black, J. H. 2005, *Astronomy and Astrophysics*, 432, 369 [3](#)
- Shirley, Y. L., Evans II, N. J., Young, K. E., Knez, C., & Jaffe, D. T. 2003, *The Astrophysical Journal Supplement Series*, 149, 375 [5](#)
- Shu, F. 1987, *Annual Review of Astronomy and Astrophysics*, 25, 23 [1](#)
- Smith, R. J., Shetty, R., Beuther, H., Klessen, R. S., & Bonnell, I. A. 2013, *The Astrophysical Journal*, 771, 24 [3](#)
- Sohn, J., Lee, C. W., Park, Y., et al. 2007, *The Astrophysical Journal*, 664, 928 [2](#)
- Sridharan, T. K., Beuther, H., Schilke, P., Menten, K. M., & Wyrowski, F. 2002, *The Astrophysical Journal*, 566, 931 [2](#), [5](#)
- Storm, S., Mundy, L. G., Lee, K. I., et al. 2016, *The Astrophysical Journal*, 830, 127 [2](#)
- Su, Y.-N., Liu, S.-Y., Li, Z.-Y., et al. 2019, *The Astrophysical Journal*, 885, 98 [5](#), [11](#)
- Su, Y., Yang, J., Yan, Q.-Z., et al. 2021, *The Astrophysical Journal*, 910, 131 [6](#)
- Sun, Y., & Gao, Y. 2009, *Monthly Notices of the Royal Astronomical Society*, 392, 170 [2](#), [5](#)
- Tan, J. C., Beltrán, M. T., Caselli, P., et al. 2014, in *Protostars and Planets VI*, ed. H. Beuther, R. S. Klessen, C. P. Dullemond, & T. Henning, 149 [2](#)
- Tang, M. Y., Qin, S. L., Liu, T., & Wu, Y. F. 2019, *Research in Astronomy and Astrophysics*, 19, 040 [2](#), [5](#), [11](#), [12](#)
- Tsamis, Y. G., Rawlings, J. M., Yates, J. A., & Viti, S. 2008, *Monthly Notices of the Royal Astronomical Society*, 388, 898 [3](#)
- Vasyunina, T., Linz, H., Henning, T., et al. 2011, *A&A*, 527, A88 [3](#)

- Wang, K., Zhang, Q., Testi, L., et al. 2014, Monthly Notices of the Royal Astronomical Society, 439, 3275 13
- Wu, J., & Evans II, N. J. 2003, The Astrophysical Journal, 592, L79 2
- Wu, Y., Qin, S. L., Guan, X., et al. 2009, Astrophysical Journal, 697, 116 5, 13
- Wu, Y., Wei, Y., Zhao, M., et al. 2004, Astronomy and Astrophysics, 426, 503 6, 14
- Wu, Y., Zhu, M., Wei, Y., et al. 2005, The Astrophysical Journal, 628, L57 3
- Xu, Y., Reid, M., Dame, T., et al. 2016, Science Advances, 2, e1600878 8
- Yang, Y., Jiang, Z.-B., Chen, Z.-W., et al. 2020a, Research in Astronomy and Astrophysics, 20, 115 5
- Yang, Y. L., Evans, N. J., Smith, A., et al. 2020b, The Astrophysical Journal, 891, 61 2
- Yorke, H. W., & Sonnhalter, C. 2002, ApJ, 569, 846 1
- Yuan, J., Li, J.-Z., Wu, Y., et al. 2018, The Astrophysical Journal, 852, 12 3
- Yue, Y. H., Qin, S. L., Liu, T., et al. 2021, Research in Astronomy and Astrophysics, 21, 14 2, 5, 11, 12, 13
- Zhang, G. Y., Xu, J. L., Vasyunin, A. I., et al. 2018, Astronomy and Astrophysics, 620, A163 3
- Zhang, Q., Sridharan, T. K., Hunter, T. R., et al. 2007, Astronomy and Astrophysics, 470, 269 3
- Zhang, S., Yang, J., Xu, Y., et al. 2020, The Astrophysical Journal Supplement Series, 248, 15 6, 14
- Zhou, S. 1992, The Astrophysical Journal, 394, 204 2, 9
- Zhou, S., Evans, Neal J., I., Koempe, C., & Walmsley, C. M. 1994, ApJ, 421, 854 1
- Zhou, S., Evans II, N. J., Koempe, C., & Walmsley, C. M. 1993, The Astrophysical Journal, 404, 232 1
- Zinnecker, H., & Yorke, H. W. 2007, ARA&A, 45, 481 1